Dipartimento di Fisica

UNIVERSITÀ DEGLI STUDI DI GENOVA

DIPARTIMENTO DI FISICA

SCUOLA DI DOTTORATO IN FISICA

CICLO XXXII

Tesi di Dottorato

Electro-Tunable Optical Devices for Molecular and Cellular Studies

Candidato: **Andrea BARBAGLIA**

Supervisore: **Dr. Francesco DE ANGELIS**

ANNO ACCADEMICO 2018/2019

Table of Contents

ABSTRACT

In the present scenario of information technology, researchers are looking for new systems able to deal more efficiently with the increasing amount of information produced by modern society. Nowadays, these tasks are accomplished by CMOS transistors and FLASH memories. Despite their wide implementation, these devices are facing serious issues along their road of development, mainly related to stable operation and power dissipation managing. Advancements in this field could boost the application of artificial intelligence and Big Data analysis, as well as enable new data communication protocols. By taking inspiration from the brain, a very powerful system characterized by low power consumption and high interconnectivity, new proposed devices, such as RRAM memories, aim at overcoming these issues. Properly engineered systems of this typology could act moreover as platforms for more precise and comprehensive biomedical studies.

In this thesis, a new class of electro-tunable optical devices is presented in the framework of next-generation memory systems. The model device possesses very favorable characteristics, such as high density and interconnectivity. Moreover, the optical readout, performed by a camera, enables parallel operation. Two realizations of this device concept were studied. The first one is a new configuration for Zero-Mode Waveguides (ZMWs), a well-known nanophotonic system used to perform studies on fluorophore dispersion at the single molecule level. In the proposed device, the interplay of an electric voltage allows to control fluorophore concentration and residence time inside the ZMWs. The light intensity coming from the ZMWs gives information about these two parameters. In the second realization, the developed ZMWs platform is used to perform an optical detection of cardiomyocytes action potentials (APs). The cells are cultured on a thin substrate placed above the fluorophore dispersion. The substrate features an array of pass-through electrodes, which allow the electric APs to be transferred from the cells to the fluorophore dispersion. APs were successfully measured with high SNR. Moreover, the device proved able to detect the effects of a drug administered to the cell culture. This device could find application as a new system for in-vitro electrophysiology, including drugs cardiotoxicity studies. Due to the optical readout scheme, it promises to offer very high spatial resolution, orders of magnitude higher than conventional multi-electrode arrays systems.

Quanti e quali siano i vantaggi di un simile strumento, tanto per le osservazioni di terra che di mare, sarebbe del tutto superfluo dire. Ma lasciate le terrestri, mi volsi alle speculazioni del cielo; e primamente vidi la Luna così vicina come distasse appena due raggi terrestri.

It would be entirely superfluous to enumerate how many and how great the advantages of this instrument are on land and at sea. But having dismissed earthly things, I applied myself to explorations of the heavens. And first I looked at the Moon from so close that it was scarcely two terrestrial semi-diameters distant.

Galileo Galilei about the telescope,
Sidereus Nuncius, Venezia, 1610.

INTRODUCTION

Nowadays, the continuous progress of technology is producing huge amounts of scientific data, thanks to always more precise and sensitive sensors, ubiquitously distributed. The integration of these data into complex models promises new exciting applications, which are expected to revolutionize our world and society in the next decades. They will involve all the different fields of science and technology: today we are just at the beginning of a new era, where information technology will permeate every aspects of our lives [1].

A popular example is given by the field of data science, whose mission is the development of new techniques for the analysis of huge and complex dataset, the so-called Big Data [2]. These methods aim at extracting valuable insights and information from "high-volume, high-velocity and high-variety" data. Moreover, by leveraging on historical series analysis, these techniques are claimed to provide predictive abilities. Besides Big Data analysis, in the last few years Artificial Intelligence (AI) has seen a significant growth [3]. The mission of AI is to replicate human intelligence in machines, in order to perform complex tasks, in a fully automated way. These tasks include perception (where the most representative example is given by pattern recognition), problem solving, learning and decision making. They will enable new powerful applications, in domains ranging from manufacturing, automotive, healthcare, robotics, entertainment, and many others. Finally, another very hot topic is given by communication technology. 5G communication networks will soon become part of our everyday life: they promise very fast data communication, enabling real-time remote control of complex equipments, as well as and the possibility to connect many different devices on the same network, realizing the so-called Internet of Things [4].

All these applications promise incredible advancements in our society. One of the fields that will benefit the most from these developments, will be the biomedical one [5]. New technological advancements are predicted to enhance the prospects of complex studies, which aim at investigating the molecular and genetic bases of diseases. The integration of these data with environmental ones are expected to give a new boost towards precision and personalized medicine. Moreover, AI is going to play a fundamental role in the development of new drugs and personalized treatments. Besides these applications, new analysis platforms will also improve the collection of biomedical data. By properly engineering their structure at the micro- and nanoscale, these systems could allow to perform studies at the single molecule or cell level. Remarkably, these devices are envisaged to offer the possibility for multi-parameter studies, where many system configurations can be investigated, by changing dynamically system's properties through external control.

Despite these sensational promises, these new technological applications have to face fundamental challenges. Besides the development of new agile and flexible algorithms, the computational resources they need for an extensive and profitable usage far exceed the present available ones. Computing and memory technology that today runs our computer, based on CMOS transistors and Flash memory, has intrinsic limits due to their structure and logic architecture. However, taking inspiration from human brain, a fascinating and incredibly efficient computational system, new computational devices are currently under development in order to overcome these limitations [6], [7]. The field is very competitive and involves both academic and industrial entities: a significant breakthrough could possibly open new ways of dealing with information, with a considerable impact in many scientific fields.

In this thesis, a new class of electro-tunable optical devices that aims at offering valid solutions to these challenges will be presented. The concept device relies on the ability to transduce an external electrical stimulus into a change of the optical properties of an active material. The system features different favorable characteristics: due to its structure, it allows for the construction of dense arrays of elements, with very high interconnectivity. Moreover, the optical readout enables efficient parallel operation. For the applications that demand these features, this family of devices can become a valuable alternative in the next future. Two different realizations of the concept device were studied, from design, to fabrication and experimental measurements. In the first realization, the device was configured in arrays of Zero-Mode Waveguides (ZMWs), a well-known nanophotonic system used to perform optical studies on fluorophores in highly concentrated solutions. The new proposed system, as additional features with respect to conventional ZMWs, enables the dynamic tuning, by means of an external electrical voltage, of fluorophore concentration and residence time in the optical excitation volume. The second realization is a new device for recording the electrical activity of excitable cells, like neurons or cardiomyocytes. With respect to common electrical recording methods, like patch-clamp or microelectrode arrays, the new device is based on an optical, rather than electrical, detection. The optical read-out performed by an optical camera is expected to bring important advantages, in particular parallel operation and incredibly high spatial resolution.

In the first chapter, the model device and the two studied realizations will be thoroughly described. An introduction to Zero-Mode Waveguides and electrical methods for cellular recording will be moreover given, as well as some general physical concepts useful for understanding device operation. In the second chapter, the fabrication procedures developed for building the two devices will be illustrated, together with the optical setup used for performing the experimental measurements. In

chapter three and chapter four, the experimental results obtained for the two studied realizations will be shown and discussed.

1 CHAPTER 1 – ELECTRO-TUNABLE OPTICAL DEVICES

1.1 Computing, memories and more: present context and future challenges

Nowadays, one of the hottest topic the scientific community is facing, is the ability to manage an increasingly larger amount of data, which need to be stored and processed for a large variety of applications. Artificial Intelligence, in particular, is demanding always more and more powerful computational resources, which present technology struggles to provide.

Currently, information processing and storage are accomplished by CMOS transistors and Flash memories, which constitute the fundamental components of today's computer processors and memories. These two components form the basic units of the so-called von Neumann architecture, which establishes that information data are stored in the memory unit and passed to the processing one in order to be elaborated, in a continuous flow of data.

Both the elementary devices, CMOS transistors and Flash memories, and the von Neumann computational architecture, have intrinsic limits, which make present computational technology not suitable for future challenges. While Moore's law predicted an exponential increase in the density of transistors per chip over time by scaling their size, forefront systems are facing arduous issues, mainly concerning heat dissipation and device stable and reproducible functioning [8]. Besides this, the von Neumann architecture implies a significant amount of time and energy spent in fruitless activities, i.e. exchanging information between the memory and the processing units [9].

By taking inspiration from the nature, scientists proposed the brain as new model for next generation computational systems. Composed by an enormous number of neurons (of the order of 10^{11}), extremely interconnected one with each other ($\sim 10^{14}$ synapses), it works with striking low power consumption (20 W, on average), holding both memory and processing functions in the same physical space. In recent times, new devices were proposed with the objective to emulate synapses and neurons and create new high performance computational systems: among them, RRAM (Resistive-switching Random Access Memory, also known as Memristors), PCM (Phase Change Memory), and MRAM (Magnetic Random Access Memory) [6]. Also organic electronic materials have been investigated as components for new neuromorphic electronics: they can provide favorable features, such as low-cost, flexibility and biocompatibility [7].

Besides emulating neuronal networks, and realizing the so-called neuromorphic computing, research also received a new boost to developing systems able to interface with biological matter, like neuronal

cells in the brain [10]. Biological hybrid devices are envisaged to open up new extraordinary possibilities, but a detailed knowledge of the interface mechanisms between biological entities, like cells and biomolecules, and the integrated device, is needed and still has to be completely discovered [11].

In the following, a new type of memory system will be presented: it is based on an optical readout scheme and, as thus, it offers very interesting features, as explained below. Thanks to its structure, the new device is also suitable for other interesting applications, especially in the fields of biology, as platform for biomolecules optical analysis and cellular recording.

1.2 The device concept: aim, structure and operation

The device concept aims at transducing an electrical signal into an optical one in a two-compartment structure, as illustrated in Figure 1.1. The two compartments are positioned one on top the other: the electrical signal is envisioned to reach the device from the top compartment (or, equivalently, from the top electrode) and being transduced into an optical signal into the lower one.

For this purpose, the lower compartment has to be constituted by an active material, whose optical response can vary according to the applied electrical voltage. The optical variation can be a change in the frequency spectrum or in the intensity of a material optical quantity, such as absorbance, transmittance, reflectance or scattering. It can be, moreover, a combination of these two effects. In the case of a fluorescent active material, it can be a change of its fluorescence emission. In Figure 1.1, a variation of the intensity of the emitted fluorescence is depicted, as implemented in the devices discussed in this thesis.

The bottom substrate has to be formed by a transparent electrode: through this component, the optical variation of the active medium is monitored by lighting the system and measuring the re-emitted light.

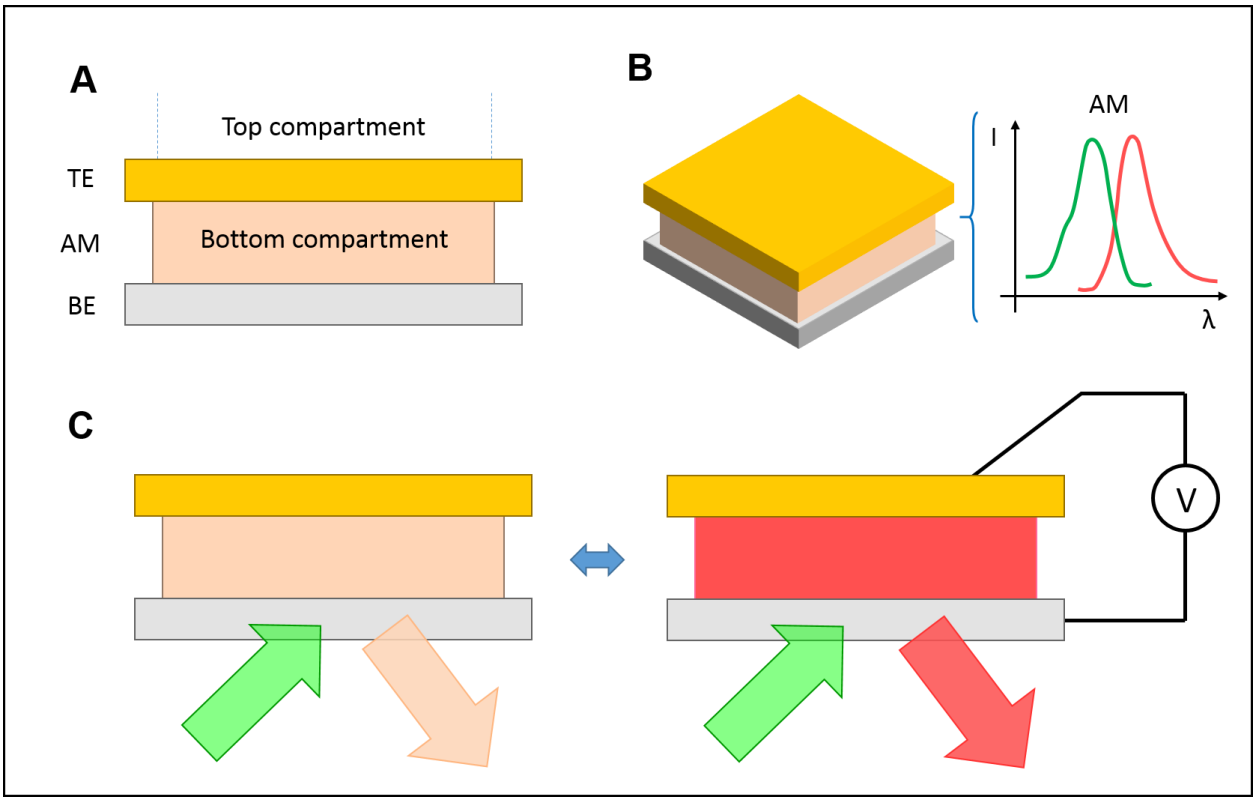

Figure 1.1. Device concept: structure and operation principle.
Schematics of the device concept, lateral (A) and 3D (B) views (TE = top electrode; AM = active material; BE = bottom electrode). In the depicted device, a fluorescent material, characterized by an absorption and emission spectra, constitutes the active material (B). (C) Device operation principle: when applying a voltage, the fluorescence light emitted by the active material changes its intensity (in the picture, an increase of the fluorescence light intensity is depicted).

A device of this typology can be of interest for many applications. In analogy with Memristors devices [12], it can be used as an optical memory, that can be reversibly written and erased by electrical pulses and read by optical means. Thanks to its layered structured, multiple devices of this kind can be arranged into a crossbar architecture, a very favorable layout, that allows for both a high spatial density and a high degree of interconnection between devices (Figure 1.2). Such kind of circuits are considered very promising for emulating neural network and performing neuromorphic computing [13].

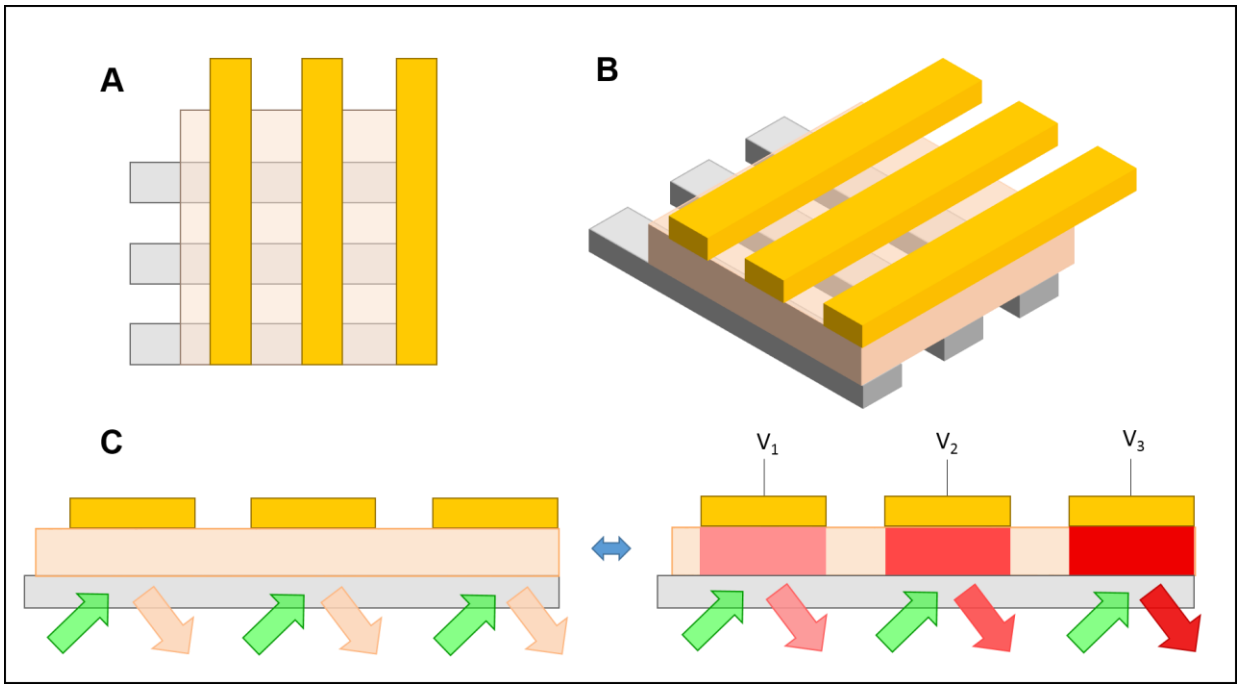

Figure 1.2. Crossbar array of devices.
Schematics of an array of devices in a crossbar architecture, top (A) and 3D (B) views. (C) Device operation principle: top electrodes are addressed individually by different electric potentials, which induce a change in the intensity of the emitted fluorescence light to different extents.

The optical readout scheme brings with it two important features: parallel operation and high bit density. Considering an array of devices, as sketched in Figure 1.3, it looks straightforward to perform the detection by an optical camera. This solution gives the possibility to monitor "at the same time" all the devices in the camera field of view (FOV) (within the limits of camera internal circuitry time constants, typically in the microsecond range). Thus, as a first non-trivial result, the optical readout allows to monitor in parallel the encoded information. Secondly, by using an optical camera, each single pixel can potentially work as a single memory bit: considering the high number of pixel modern cameras are endowed with (more than 1 million), optical readout can offer very high bit density, where the limit is set, in principle, just by light diffraction.

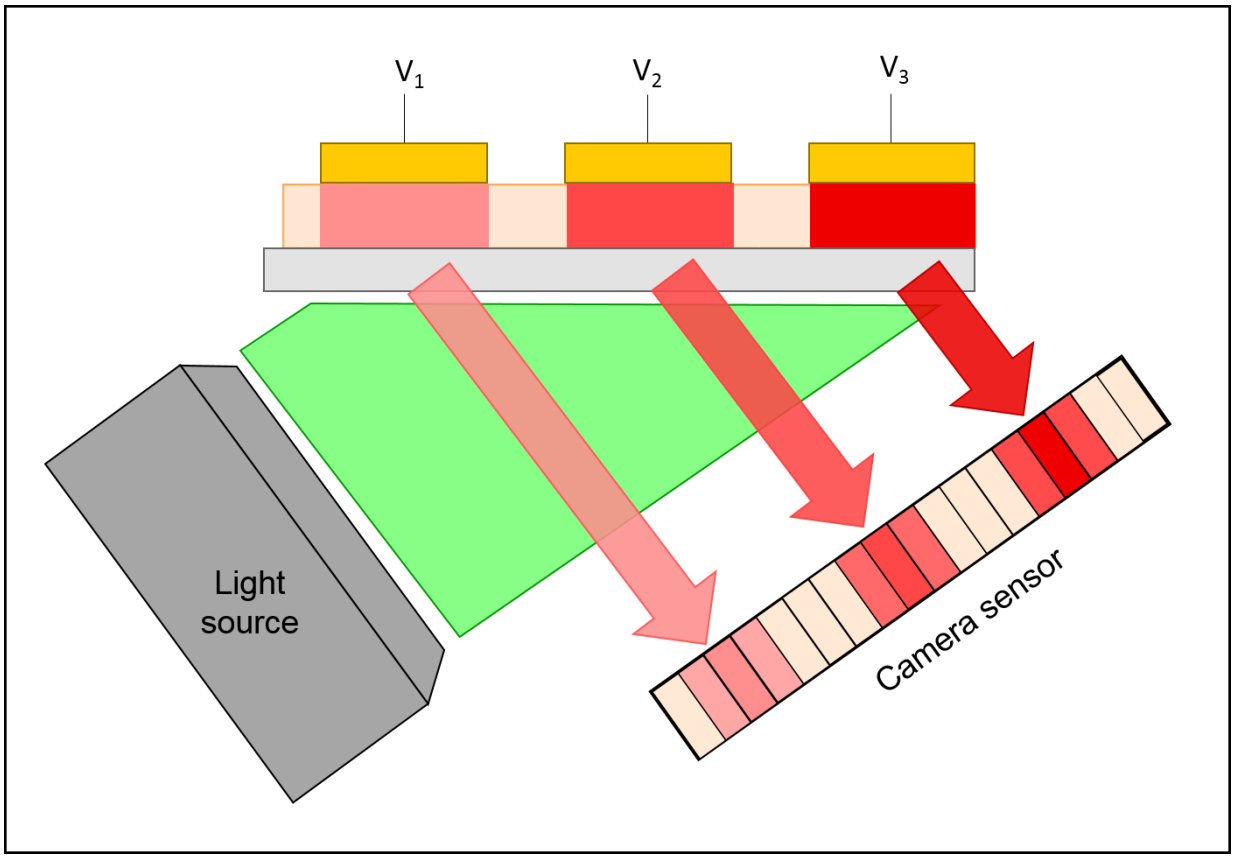

Figure 1.3. Schematics of system functioning.
A light source illuminates the system, while the top electrodes drive independently the active medium. The re-emitted light is collected by the megapixel sensor of an optical camera, which allows for devices parallel detection, and enables for high bit-density memories.

From another point of view, this model device can represent a tunable metasurface, to be used in photonic circuits as, for example, a tunable filter, mirror, lens or polarizer [14], [15]. Both for the memory and the metasurface applications, non-volatility and fast switching are highly desired features.

Remarkably, this device could also find application as platform for optical analysis of molecules or bio-chemical reactions in liquid environment. In this configuration, the active material is substituted with the sample dispersion, and the external voltage is expected to allow the control of relevant sample's parameters in the optical volume of analysis (e.g. molecule concentration, electrodes potential for electrochemical reactions,…).

In literature, several examples of this class of devices can be recognized, having structures that can be reduced to the one depicted in Figure 1.1, but working principles based on different physical phenomena. Liquid crystals and phase change materials are well known active materials that can

change their optical response depending on the applied electrical voltage: during the last decades, they became a well-establish technology respectively for optical displays and optical storage systems. In more recent years, they have been employed as components for new hybrid waveguides or plasmonic metamaterials, in order to allow the dynamic control of their optical properties [16], [17]. Another example of electro-tunable device is given by electrochromic materials, whose most promising applications are found in the field of architecture as smart windows [18].

In order to explore new possibilities of tuning optical behavior at striking low voltages, researchers started to investigate new original classes of active materials, like for example dispersion of nanoparticles. In [19], the voltage-controlled self-assembly/disassembly of a layer of gold nanoparticles at the interface between two immiscible liquid solutions is shown to modify the reflectance intensity and spectrum at few hundreds mV. In another work [20], the reversible trapping by dielectrophoresis of polystyrene, quantum dots and diamonds nanoparticles, at biases as low as 100 mV, is demonstrated and proposed as principle for new nanophotonic devices. As a last example, in [21] the voltage-controlled nucleation and growth of metal nanoparticles induces measurable changes in the reflectance spectrum at biases as low as 5 mV. All these materials and devices are considered very promising for new low-power-consuming opto-electronics systems.

In the following sections, the realization of two different electro-tunable optical devices belonging to this class of systems will be presented. The first proposed device finds application in the field of optical studies of fluorophore dispersions at the single- or few-molecules level. The second proposed device, on the other hand, will consist in a new platform for recording, optically, the electrical activity of electrogenic cells.

1.3 Electro-Active Zero-Mode Waveguides

The first device presented in this thesis is a new configuration for Zero-Mode Waveguides (ZMWs), a passive system developed to perform optical studies at the single molecule level in highly concentrated solution [22]. In the new device, an applied electrical voltage is expected to tune fluorophore concentration and residence time in the optical excitation volume: for this reason, the device will be named Electro-Active Zero-Mode Waveguides (EA-ZMWs).

In the following section, an introduction to ZMWs will be given. Thereafter, the new developed device will be described in its concept and operation principle.

1.3.1 Zero-Mode Waveguides

Zero-Mode Waveguides are well-known optical nanostructures used to confine light in an extreme subwavelength volume, thus enabling to detect from few to single fluorescent molecules in highly concentrated solutions. They have been initially introduced to improve optical approaches for DNA sequencing and then used in a wide variety of applications, for example monitoring of bio-chemical reactions at the single molecule level [23].

Namely, they consist of subwavelength nanoholes drilled in a thick metallic film on a transparent substrate, where molecules can flow in and be detected (Figure 1.4). By lighting the system from below, the incoming light with wavelength above a critical threshold λ_c will not propagate inside the ZMWs: only evanescent waves will penetrate, decaying exponentially along the waveguide axis. The cut-off wavelength λ_c depends on nanoholes' shape and size: in the general case of a circular waveguide of diameter d in a perfect conductor, it follows that $\lambda_c = 1.7\mathrm{d}$. Incident light with $\lambda_m > \lambda_c$, where λ_m is the wavelength in the medium composing the core of the waveguide, will decay according to:

$$I(z) = I(0)e^{-z/\Lambda}, \text{ where } \frac{1}{\Lambda} = 2\sqrt{\frac{1}{\lambda^2} - \frac{1}{\lambda_m^2}}.$$

This condition allows to reach very small excitation volumes inside the nanoholes, from atto-Liter to zepto-Liter (aL ÷ zL), between 2 to 5 orders of magnitude smaller than a diffraction-limited light volume, that can be estimated around 0,2 femto-Liter (fL). As a consequence, single-molecule level can be reached at much higher concentrations, passing from values between pM and nM in the case of diffraction-limited optics, to concentration values in the μM ÷ mM range, at which typical bio-chemical reactions occur.

The most common metals used for ZMWs fabrication are aluminum and gold, used also in combination [24]. Aluminum is characterized by a high and broad reflectivity and short optical skin depth; on the other hand, gold shows high resistance to oxidation, can provide plasmonic enhancement, and enables the using of an extensive surface binding chemistry (i.e. the thiol-based chemistry) to confer functionalities to the ZMWs surface. ZMWs nanoholes are typically made via electron-beam lithography or focused ion-beam milling: they generally have lateral size between 40 and 150 nm.

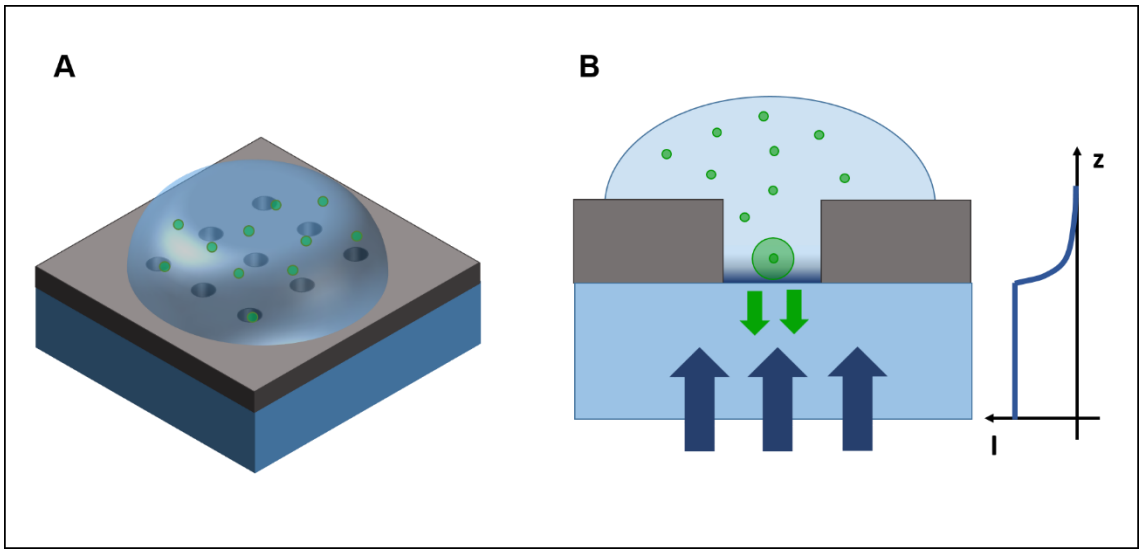

Figure 1.4. Schematics of ZMWs.
(A) Array of ZMWs with a drop of fluorophore dispersion on top. (B) Cross-section view of a single ZMW, and profile of incident light intensity: the light evanescent field decreases exponentially in the nanohole volume, exciting single fluorescent molecules.

It is worth to note that ZMWs nanoholes, typically fabricated at a relative distance of some micrometers, can be measured in parallel, i.e. at the same time, by using an optical camera. This feature represents a significant improvement with respect to other techniques for single-molecule optical studies, like Scanning Near-Field Optical Microscopy (SNOM), where the optical excitation volume is localized under the nanophotonic probe and a scanning procedure is required to image the whole sample [25]. If compared to TIRF (Total Internal Reflection Fluorimetry) microscopy, another optical technique based on light confinement, ZMWs allow to obtain a confined light volume also in the x-y plane and not just in the z direction [26].

1.3.2 The new proposed device: EA-ZMWs

ZMWs represent a very powerful system for studying highly concentrated fluorophore dispersion at the single- or few-molecules level. Nevertheless, ZMWs so far described in literature operate at fixed fluorophore concentration that, moreover, has to be properly tuned in order to reach single-molecule level inside the nanoholes.

In order to overcome this limit, a new configuration for ZMWs was developed, following the device paradigm depicted in Figure 1.1. In the new device, the bottom substrate is a transparent electrode, as for example an ITO (Indium Tin Oxide) coated glass, and the considered fluorophores are electrically charged (Figure 1.5).

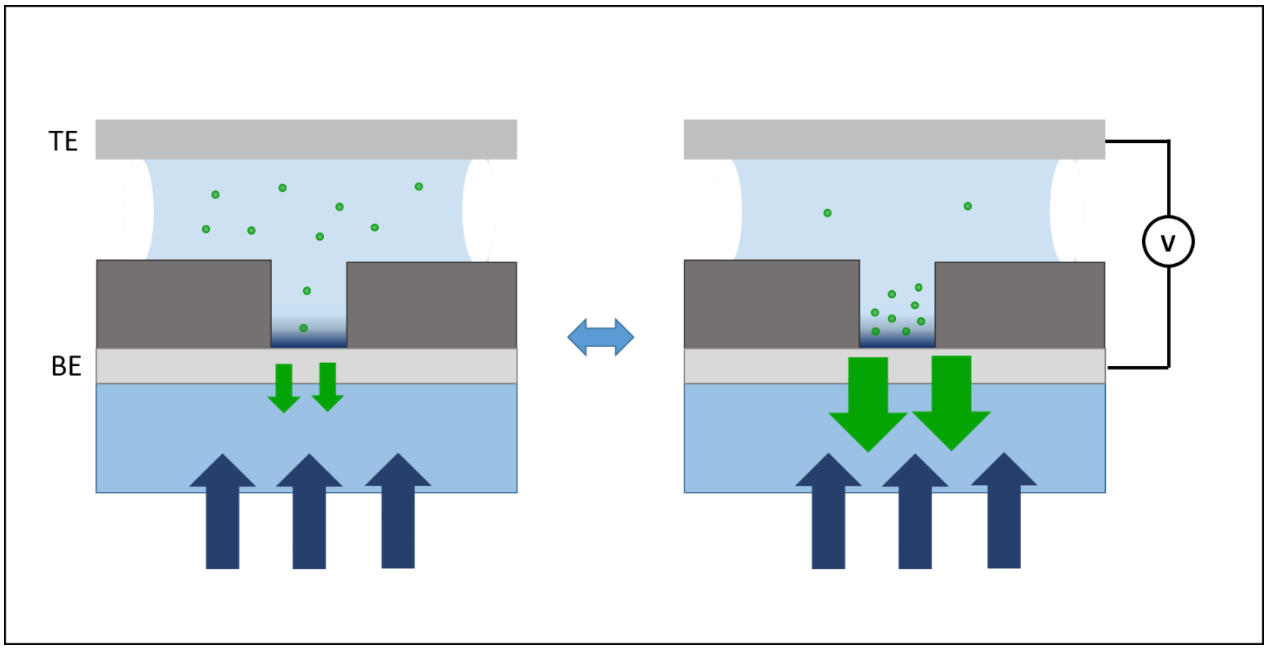

Figure 1.5. Schematics and operation principle of EA-ZMWs device.
The applied voltage between the top (TE) and the bottom (BE) electrodes allows to drive fluorophores in-and-out the ZMW, enabling to tune their concentration and residence time inside the optically active volume.

Through the application of an external voltage between the bottom ITO layer and a counter electrode placed on top of the device, fluorophores are expected to be driven in-and-out the nanoholes by the applied electric field, modifying their concentration in the optically active volumes. This dynamics is expected to generate (and thus be monitored by) a variation of the light intensity emitted from the nanoholes. Through this approach, different experimental conditions, characterized by different fluorophore concentrations, are expected to be realized and tested in the same device, in a fully dynamic and convenient way.

Importantly, the external voltage is also expected to enable the control of fluorophore residence time inside the nanoholes, giving thus the possibility to regulate the time duration of the event under investigation.

1.4 Optical recording of cardiomyocytes action potentials

The second device proposed in this thesis aims at recording the electrical activity of cultures of excitable cells, like neurons or cardiomyocytes, by converting their electrical activity into optical signals.

Among excitable cells, neurons are matter of great interest being the elementary components of our brain, a very complex and powerful system, studied not only for biomedical reasons, but also as a model for new, more efficient, computational circuits. New methods for studying and interfacing with neurons could open the path to new scientific and technological discoveries, with a strong impact in many fields.

On the other hand, the field of new methods for cardiomyocytes recording is drawing increasing importance, especially in the pharmaceutical community. Among their applications, these systems are employed for drugs screening on cells, with the objective to reveal possible toxic effects at a very prior stage in the drug approval process. New methods, always more precise, are strongly demanded, as they may speed up the drugs development pipeline, reducing costs and increasing efficiency.

The device here presented was tested with cardiac cells. In the following sections, a description of cardiomyocytes action potentials and relative electrical recording methods will be given. Subsequently, the new developed device will be presented in its structure and operation principle.

1.4.1 Cardiac cells and action potentials

Cardiac cells (or cardiomyocytes) are excitable (also called electrogenic) cells (ECs) due to their ability to respond to (and generate) electrical signals. The electrical signal they generate and communicate with is called action potential (AP) and is associated with a contractile motion [27].

Cardiac cells are usually divided into two categories: pacemaker and non-pacemaker cells. Pacemaker cells, also called sinoatrial node (SAN) cells, have the ability to spontaneously produce APs, and therefore initiate the contractile activity. In healthy heart, SAN is found in the right atrium and produces roughly 60-100 APs per minute, that correspond to a resting heart rate of roughly 60-100 beats per minute. Beating rate is a very important parameter, whose alteration can lead to severe cardiac diseases, including cardiac arrhythmia.

Non-pacemaker cells, among them atrial and ventricular cells, cannot generate APs, but only propagate the APs they receive from surrounding cells, together with the contractile motion. The propagation of the AP from one cell to the other is mediated by specific intercellular connections,

called *gap junctions*: they connect the cytoplasm of two cells, allowing the cells to exchange ions and thus transfer the AP.

APs of pacemaker and non-pacemaker cells have slightly different features [28]. In the following paragraph, a general description of cardiomyocytes APs will be given, referring mainly to non-pacemaker cells.

Cardiomyocytes action potential

An AP is a reversible change of the membrane potential caused by a sequential activation of several ion currents, generated by the diffusion of ions through the ion channels in the cellular membrane. The membrane potential is calculated as the difference between the inner membrane potential and the outer membrane potential: at rest, this difference is more or less constant and equal to roughly -85 mV, which means that the interior side of the membrane has lower potential with respect to the outer side. When an AP is triggered, membrane potential moves to positive values up to +20 or +30 mV (depolarization process), and then recovers back to the basal resting membrane potential (repolarizing process). A total amplitude of 110 mV can be calculated for a single AP.

From a biochemical point of view, the process is quite complicated and involve mainly 3 types of ions (Na^+, K^+, Ca^{2+}) and transmembrane proteins that act as ions channels or ionic pumps. In the scientific literature, the AP is commonly described by 5 phases (from phase 0 to phase 4) [29]. As an example, the AP shape of a non-pacemaker ventricular cell is depicted in Figure 1.6.

While phase 0 (depolarization) and phase 3 (repolarization) are rapid phases, the intermediate phase 2, also known as plateau phase, is the main responsible of the AP time duration. At physiological conditions, the total time duration of a healthy cardiomyocyte AP can be estimated of the order of 200 ÷ 500 ms according to the type of cardiomyocyte.

AP shape and time duration are very important parameters to monitor during electrophysiological studies: their alteration can be sign of a heart pathology, and their precise measurement can give important insights towards the understanding of the biomolecular causes. On the other hand, also medical drugs can affect cardiac cells activity, and their possible side affects can be revealed as modifications in AP shape and time duration [30].

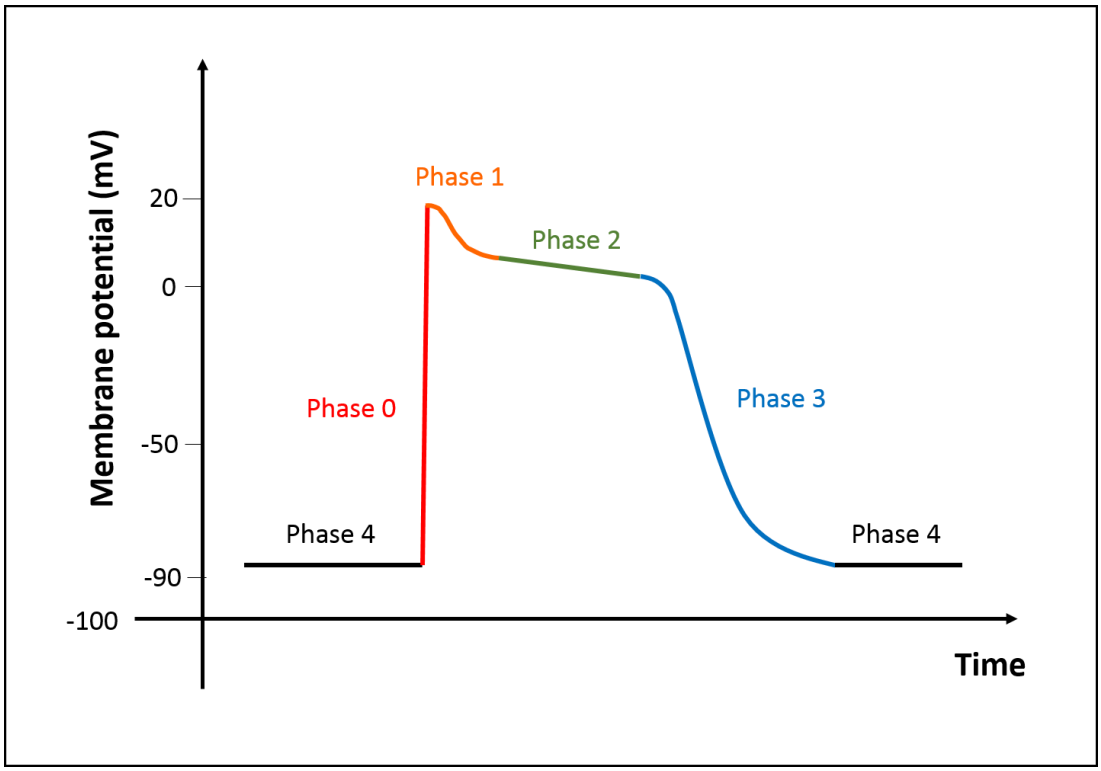

Figure 1.6. Typical profile of a non-pacemaker ventricular cardiomyocytes action potential.
The AP shape is divided according to five different phases: in phase 4, the cell is at its resting potential; phase 0 is also known as depolarization phase; phase 1 is the first phase of the repolarization process; phase 2 is also known as plateau phase; in phase 3 rapid repolarization takes place.

1.4.2 Electrical recording methods

During the last decades, different methods have been developed in order to perform in-vitro direct monitoring of the electrical activity of excitable cells, including, in the special interest of this thesis, cardiomyocytes. These systems make use of electrodes that directly interface with cells, in order to capture membrane potential variations, as APs above described.

Recorded APs can have different amplitude and shape, depending on the electrical coupling between the cell and the electrode. In particular, a huge variation in the AP is measured when the electrode passes through the membrane and comes into contact with the intracellular medium. In this case, recorded APs can reach much higher amplitude and longer time duration, and faithfully retrace the shape depicted in Figure 1.6: these recorded APs are typically referred to as intracellular APs, in opposition to field potentials, recorded when the electrode remains in the extracellular environment. In Figure 1.7, commonly recorded shapes for intracellular APs and field potentials are reported, together with their typical time and amplitude scales [31].

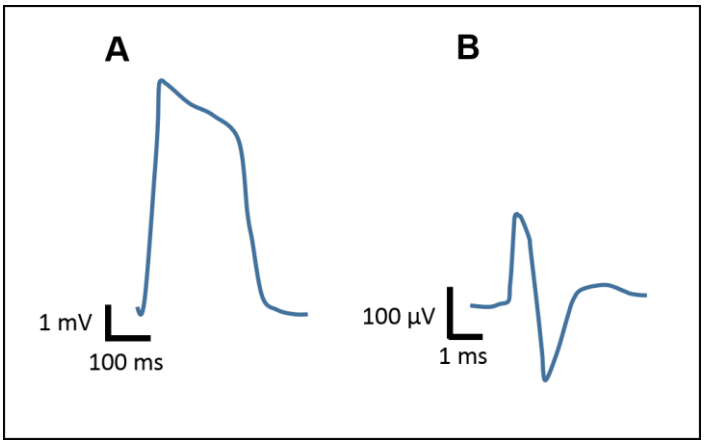

Figure 1.7. Commonly recorded signals for intracellular APs and field potentials by electrical recording methods.
Typical signals recorded from cardiomyocytes by means of electrical recording methods: A) common shape of a recorded intracellular AP; B) common shape of a recorded field potential.

In the following, the two most relevant methods for in-vitro APs direct electrical monitoring will be described, together with the information they can provide and some recent breakthroughs: the patch-clamp technique and the MEA and CMOS-MEA systems.

1.4.2.1 Patch-clamp

The patch-clamp technique is considered the benchmark among all recording methods, as it allows to measure directly the current (or voltage) associated to an AP [32]. Through a micropipette (or patch-pipette) electrode, filled with an electrolyte solution, a small region of the cellular membrane is selected (the "patch"), where only one or few ionic channels are present. In the most common patch-clamp configuration, this is obtained by pressing the micropipette against the surface of the cell membrane and applying a gentle suction. As a consequence, the membrane curves inside the pipette forming an omega-shaped junction, characterized by a very high resistance with the external bath (10-100 GΩ). This high resistance, called "seal resistance" or "gigaohm seal", allows to isolate electrically the membrane patch, which means that all the ions flowing through that portion of the membrane into the micropipette are recorded by the electrode, with little competing noise. Additionally, the tight seal between the micropipette and the electrode provide mechanical stability to the recording process.

The recording operation is usually performed by applying a set voltage between the micropipette electrode and the bath, and measuring the current then injected into the system to preserve this potential value (voltage-clamped mode). This current will be opposite in sign and equal in magnitude to the current flowing through the membrane, resulting from AP propagation. On the other hand, the

current-clamped modality imposes a current flowing into the system and measures the required voltage to preserve this current. In this case, voltage variations generated by cellular AP are recorded.

The patch-clamp technique is susceptible to many variations, according to the type of junction the experimenter creates at the interface between the micropipette and the cell. When more suction is applied, the small patch of membrane can be displaced: the micropipette remains sealed to the rest of the cell and the electrode is now in direct contact with the intracellular medium. In this configuration, known also as "whole-cell" mode, intracellular recording can be performed.

Patch-clamp is a very powerful technique as it is very sensitive to small variations of the membrane electrical voltage and because it allows to investigate cellular electrical behavior at the single ionic channel level. On the other hand, it has a very low throughput, as it allows to measure only one cell at a time, and, due to mechanical and biophysical instabilities, cannot be used to perform long-term electrophysiological measurements. As another drawback, in the "whole-cell" mode, where intracellular recording is made possible, cytoplasm mixes with the micropipette solution: intracellular fluid ions can be diluted and the recording can be less reliable.

1.4.2.2 MEA and CMOS-MEA

Microelectrode arrays (MEAs) and CMOS-based microelectrode arrays (CMOS-MEAs) represent well established techniques for extracellular recording of field potentials, but their recent developments appear very attractive and promising also for intracellular measurements. MEAs devices consist of multiple (tens to few hundreds) passive microelectrodes connected to the external circuitry by conductive feedlines and contact pads [33]. CMOS-MEAs, on the other hand, feature thousands of electrodes, along with integrated readout and stimulation circuits on the same chips [34]. MEAs and CMOS-MEAs devices exist both for in-vivo and in-vitro measurements.

In in-vitro MEAs and CMOS-MEAs studies, cells (or tissue slices) are cultivated (or positioned) on top of the electrodes. When the cells become electrically active and start to fire APs, the corresponding change in voltage, caused by transmembrane ionic currents, is transduced into electronic currents inside the MEAs electrodes. The recorded signals have size and shape that depend on several factors: the tightness and the contact area between cells and MEAs electrodes; the nature of the medium in which the cells are located (electrical conductivity, dielectric capacitance); and the electrical characteristic of the MEAs electrodes themselves (geometry, impedance and noise). Analog signal processing and data sampling processing parameters have to be carefully adjusted in order to obtain a good electrical recording.

In recent years, by endowing MEAs electrodes with sharp 3D nano- or micro-structures, intracellular APs have been also successfully recorded. Sharp tips and nanostructures have been demonstrated to penetrate cellular membrane without significantly affecting cell viability. In some cases, this phenomenon can happen spontaneously, according to the geometry of the structures [35], [36]. In other cases, electric or laser pulses can be used to promote the formation of transient pores through the membrane, in correspondence of the nano-/microstructures: these processes are known, respectively, as electroporation [37], [38] and optoacoustic poration [39], [40]. Such a modification of the membrane allows electrodes to be in direct contact with the intracellular compartment and thus to measure intracellular APs.

If compared with patch-clamp technology, MEAs and CMOS-MEAs have the considerable advantage of being able to record signals from a very large population of cells, all the same time. Besides increasing the throughput of measured APs, this feature allows also to measure and characterize signal propagation across the cellular culture. On the other hand, recorded APs have usually lower signal-to-noise ratio (SNR) with respect to patch-clamp measurements, due to the looser coupling with cells and the higher noise coming from the circuitry.

1.4.3 The new proposed device: CORE device

The second device proposed in this thesis aims at performing an optical recording of the electrical activity of excitable cells, by taking advantage of the device paradigm described in Section 1.2. It will be named in the following CORE device (Cells Optical REcording device): its schematics and operation principles are described in Figure 1.8.

In this device, cells are the sources of the electrical voltage: they are located in the top compartment, above the top electrode, which collect their electrical signals and transfer them to the bottom compartment. Here, the electrical signals are expected to modify the optical response of the active medium, to be monitored by an optical camera. It is worth to note that the active medium has to be sensitive to variations of the electrical voltage at least of the order of the AP amplitude, equal to approx. 110 mV.

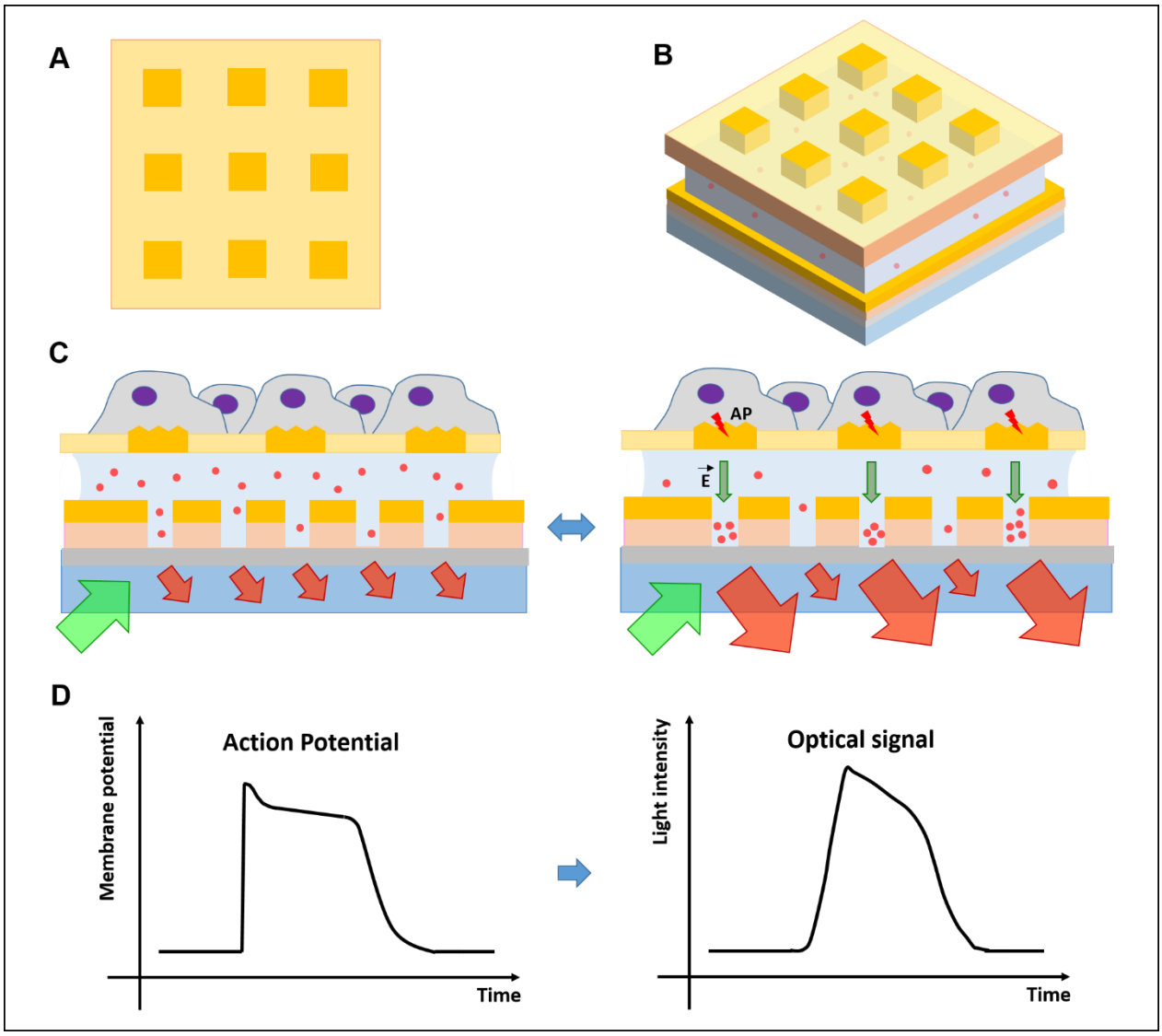

Figure 1.8. Schematics and operation principle of CORE device.
Schematics of CORE device, top (A) and 3D (B) view: the top electrode is constituted by a series of passing-through independent electrodes in a thin insulating layer. (C) Device operation principle: when cells in the upper compartment fire their APs, the underlying electrodes polarize. The generated electric field is expected to push fluorophore molecules in-and-out the bottom electrode ZMWs. The optical signals coming from the ZMWs are monitored by an optical camera (see also Figure 1.3). (D) By relying on this operation principle, the device is expected to transduce cells APs into optical signals.

The interface between the two compartments has to be properly designed in order to offer both good coupling with cells and an efficient transmission of their electrical signals to the underneath medium. A series of passing-through independent electrodes in a thin insulating layer can be envisioned as possible embodiment. In order to enhance both the mechanical and electrical coupling with the cells on top, the electrodes upper surface can be decorated with 3D micro-/nanostructures or endowed with

an increased roughness. As demonstrated by a number of studies, these surface topologies can favor cellular adhesion and, consequently, electrical coupling: SEM analysis show that cells tend to protrude their membrane inside wrinkles and pores, or to literally engulf micro-/nanostructures, establishing a very close contact between their membrane and the underlying electrode [41].

The fired cellular APs are expected to polarize the electrodes, which the cells are coupled with, and thus be transferred to the lower compartment. In the proposed device realization, the active medium is a dispersion of charged fluorophore and the bottom electrode is made by arrays of Zero-Mode Waveguides, of the type described for the EA-ZMWs device. In the lower compartment, the polarized electrodes are predicted to generate an electric field able to push fluorophore molecules in-and-out the ZMWs. As explained for the EA-ZMWs device, this motion will result in light signals coming from the ZMWs. These optical signals are linked to the cellular APs originating the electric field in the active medium. Thus, by monitoring these signals by means of an optical camera placed underneath the device, an optical map of the fired APs is expected to be measured in time. The recorded light signals may show some differences in their shape and time duration with respect to the initial cellular APs (see Figure 1.8 D): such deviations could origin from fluorophores dynamics during the AP transduction process. Nevertheless, by modeling fluorophore dynamics, a correction factor should be derived, which, once applied to recorded optical signals, could allow to retrieve actual cellular APs.

With respect to the renowned recording methods of patch-clamp and microelectrodes arrays, the new method is expected to offer a simpler and less costly detection, performed just by using an optical camera. Moreover, the optical readout will give the possibility to detect in parallel, i.e. during the same acquisition process, all the electrodes in the camera FOV (AP signals occur on time scales much longer than common CCD or CMOS camera internal circuits time constants). As a further advantage, considering the very high number of pixel modern camera sensors are endowed with (more than 1 million), the map of fired APs is foreseen to be recorded as a continuous map, with an extraordinary high spatial resolution. In the limit of maximum spatial resolution, each single pixel is an AP detector and the spatial resolution limit is set just by light diffraction. Finally, combining both parallel detection and the very large number of available pixel sensors, according to the optics magnification used, large throughput is enabled, preserving high spatial resolution.

1.5 Physics background

In this section, some physical concepts useful to describe the functioning of the two devices above presented will be briefly summarized. They will mainly deal with the dynamics of charged particles in fluids under the application of an external electric field.

1.5.1 Diffusion and electrical mobility

Diffusion motion

Atoms and molecules in solution undergo a random motion resulting from their collision with the fast moving molecules of the fluid [42]. This phenomenon is known as Brownian motion and was theoretically described by Einstein in 1905. The relation

$$\langle r^2 \rangle = 2Dt \tag{1.1}$$

links the mean square displacement of a single particle to the diffusion coefficient D and the elapsed time t. The Stokes-Einstein relation shows how the diffusion coefficient D depends on the particle hydrodynamic radius r and the solvent viscosity η:

$$D = \frac{k_B T}{6\pi r \eta} \tag{1.2}$$

where k_B is the Boltzmann constant, T is the absolute temperature, and the pre-factor 6π is relative to a spherical approximation of the particle shape.

In the presence of a concentration gradient, particles are also subjected to a diffusion motion, superimposed to the Brownian one, from regions of high concentration to regions of low concentration. The two Fick laws describe this effect from a macroscopic point of view.

The first Fick law links the diffusive flux J to the concentration φ in the assumption of steady state:

$$\boldsymbol{J} = -D\nabla\varphi \tag{1.3}$$

As described above, this relation establishes that particles move from regions of high concentration towards regions of low concentration and their flux is proportional to the concentration gradient.

The second Fick law describes how the particle concentration changes with respect to time as a consequence of particles diffusion:

$$\frac{\partial \varphi}{\partial t} = D\nabla\varphi \tag{1.4}$$

Typical values for the diffusion coefficient of ions in water at 25°C are of order of 10^{-5} cm^2/s.

Electrical mobility

When an electrical voltage is applied to an electrolyte solution, each ion of a given species *i* is subjected to a force *F* proportional to the applied electric field *E*:

$$F_i = z_i q E \tag{1.5}$$

where z_i is the number of charge of the species *i* and *q* is the elementary charge.

In a simplified picture, solvent molecules tend to hinder ions motion. The Stokes law describes this effect through a force F_S opposite to (1.5) and proportional to the ion velocity *v*:

$$F_{S,i} = 6\pi r_i \eta v_i \tag{1.6}$$

where *r* is the ionic hydrodynamic radius, η is the solvent viscosity and the pre-factor 6π is again due to a spherical approximation for the ion size.

The system dynamics, expressed by the two forces (1.5) and (1.6), states that ion velocity increases up to a constant value, called drift velocity v_D, equal to:

$$v_{D,i} = \frac{z_i q}{6\pi r_i \eta} E = \mu_i E \tag{1.7}$$

where the pre-factor:

$$\mu_i = \frac{z_i q}{6\pi r_i \eta} \tag{1.8}$$

is called electrical mobility of the species *i*, and describes the ability of a given ion to move through a solvent in response to an electric field.

Typical electrical mobilities of ions in water are of the order of $5 \cdot 10^{-4}$ cm^2/Vs (as an example, for Na^+, $\mu = 5.19 \cdot 10^{-4}$ cm^2/Vs).

When considering different solvents, ions electrical mobility (as well as ions diffusion coefficient, see equation 1.2) can change according to the solvent viscosity. As an example, ethylene glycol has viscosity around 20 times higher than water, thus ions or molecules are expected to move slower in ethylene glycol than in water (ethylene glycol viscosity = 16.2 mPa·s; water viscosity = 0.89 mPa·s).

From the drift velocity, it is possible to compute the current density *J* given by the ions *i*:

$$J_i = z_i q c_i v_{D,i} = z_i q c_i \mu_i E \tag{1.9}$$

where c_i is the volume concentration of ions *i*.

By summing up the contributions of all the ionic species, it is possible to compute the total current density:

$$J = \sum_i z_i q c_i \mu_i \, E = \sigma E \tag{1.10}$$

The coefficient σ is the electrical conductivity of the medium. The inverse of σ is the electrical resistivity ρ:

$$\rho = \frac{1}{\sigma} = \frac{1}{\sum_i z_i q c_i \mu_i} \tag{1.11}$$

These values, σ and ρ, describe the mean electrical properties of the electrolyte solution under study.

1.5.2 The electrochemical double layer

At the interface between a metal electrode and an electrolyte, electrochemical reactions can occur, that will result in the formation of a potential difference between the two media, and a relative charge on the electrode surface [43]. As a result, anions and cations in solutions respond to the generated potential difference, leading to an accumulation of oppositely charged ions at the electrode surface, until the excess charge is compensated. The two layers with opposite electric charge are named electrochemical double layer.

The same phenomenon originates when an external voltage is applied between the electrode and the electrolyte: the potential drops across the interface and reaches a constant value in the bulk electrolyte. To describe how the potential varies between the two media, the Stern model gives a detailed picture (Figure 1.9).

This model identifies two regions with different charge distributions inside the electrolyte. In the first region, ions with opposite charge are distributed along a plane facing the electrode. This plane is called Helmholtz plane. Since the model considers ions as particles with finite size, they cannot approach the surface any closer than their ionic radius. On the other hand, the second region extends into the electrolyte, where ions form the so-called diffuse layer.

As a consequence of this picture, the potential drop shows a linear profile in the first region, and a slower decay into the second one, that can be approximated by an exponential function:

$$\begin{gathered} x < a: \;\; \Phi_x = \Phi_e - \frac{\Phi_e - \Phi_H}{a} x \\ x \geq a: \quad \Phi_x \approx \Phi_H \, e^{-\kappa(x-a)} + \Phi_b \;\; \text{(valid for } \Phi_H \leq 50 \text{ mV at 25°C)} \end{gathered} \tag{1.12}$$

where a is the position of the Helmholtz plane, Φ_e is the electrode potential, Φ_H is the potential at the Helmholtz plane, Φ_b is the potential in the bulk of the electrolyte solution.

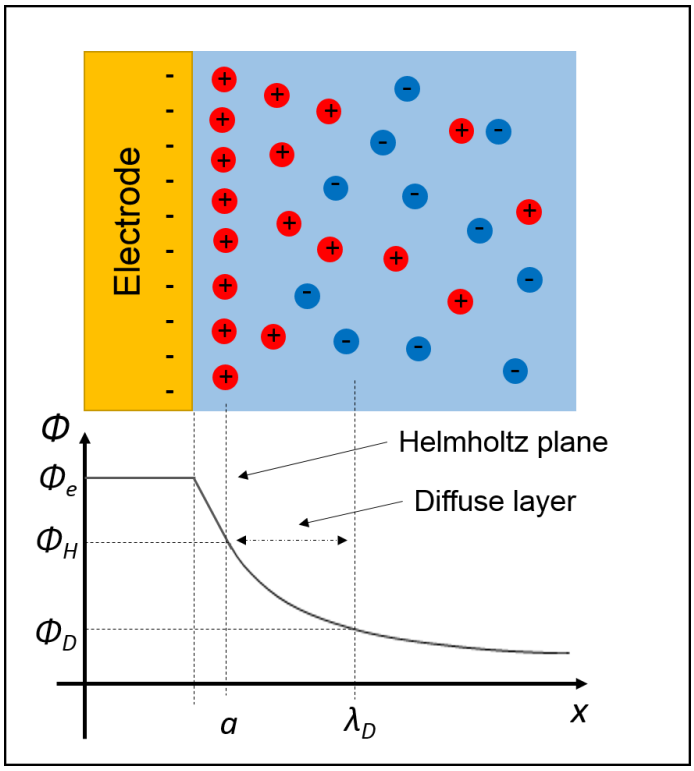

Figure 1.9. Stern model for the electrochemical double layer.
Pictorial representation of ions distribution and potential profile Φ in the electrolyte solution. The potential drop is linear till the Helmholtz plane, located at position a, then it can be approximated by a negative exponential function (Φ_e electrode potential, Φ_H Helmholtz potential, Φ_D potential at the Debye length, λ_D Debye length).

The characteristic decay length of the potential in the diffuse layer, also known as Debye length $\lambda_D = \kappa^{-1}$, is described by the following formula:

$$\lambda_D = \kappa^{-1} = \sqrt{\frac{\varepsilon_r \varepsilon_0 k_B T}{2 N_A e^2 I}} \tag{1.13}$$

where ε_r is the relative dielectric permittivity of the medium, ε_o the vacuum dielectric permittivity, k_B the Boltzmann constant, T the absolute temperature, N_A the Avogadro number, e the elementary charge and I the molar ionic strength of the solution. The molar ionic strength is defined as:

$$I = \frac{1}{2}\sum_{i=1}^{n} c_i z_i^2 \tag{1.14}$$

where c_i and z_i are the molar concentration and the charge number of the i-th ionic species. According to equations 1.12, 1.13 and 1.14, by increasing ions concentration, the potential drops more rapidly as a consequence of the reduction of the Debye length. Table 1.1 reports the values for λ_D in pure deionized water and in different aqueous solution of NaCl at 25°C.

	Pure deionized water	NaCl 0.01 M	NaCl 0.1 M	NaCl 1 M
λ_D (nm)	960	3.0	0.96	0.30

Table 1.1. Debye length and ionic strength.
Debye length of pure deionized water and aqueous solutions of NaCl with different molar concentrations, computed according to equations (1.13) and (1.14).

From an electrical point of view, the whole system can be modeled by two capacitances connected in series, a Helmholtz layer capacitance C_H and a diffuse layer capacitance C_D. Their inverse can be summed up in order to obtain the composite double layer capacitance C_{dl}.

$$\frac{1}{C_{dl}} = \frac{1}{C_H} + \frac{1}{C_D} \tag{1.15}$$

Typical values for the double layer capacitance are in the range $10 \div 40$ μF/cm^2.

In systems where electrochemical reactions can occur between the electrode and the electrolyte, a flow of electrons (i.e. a current) originates between the two media. This effect is modeled by adding an electrical resistance in parallel to the double layer capacitance.

1.5.3 The electrochemical cell

According to its most simple definition, an electrochemical cell is a device formed by two electrodes separated by an electrolyte [44]. By applying a voltage between the two electrodes, the electric field induces a motion of ions in solution, i.e. a current: as shown in Figure 1.10 A, this cell behavior can be modeled by a parallel of an electrical capacitance and a resistance.

As explained in the previous paragraphs, ions motion causes the formation of two double layers at the electrode interfaces. In the absence of any charge transfer at the electrodes surfaces, ions will screen the electrodes charges and the current generated by ions motion will tend to zero. Conversely, in the case of electrochemical reactions between the electrodes and the electrolyte, a current will continue to flow inside the cell. In this second more general description, electrodes interfaces are modeled by a parallel between a capacitance and a resistance, where the capacitance describes the effect of the double layer, while the resistance, the current flowing due to electrochemical reactions (Figure 1.10 B).

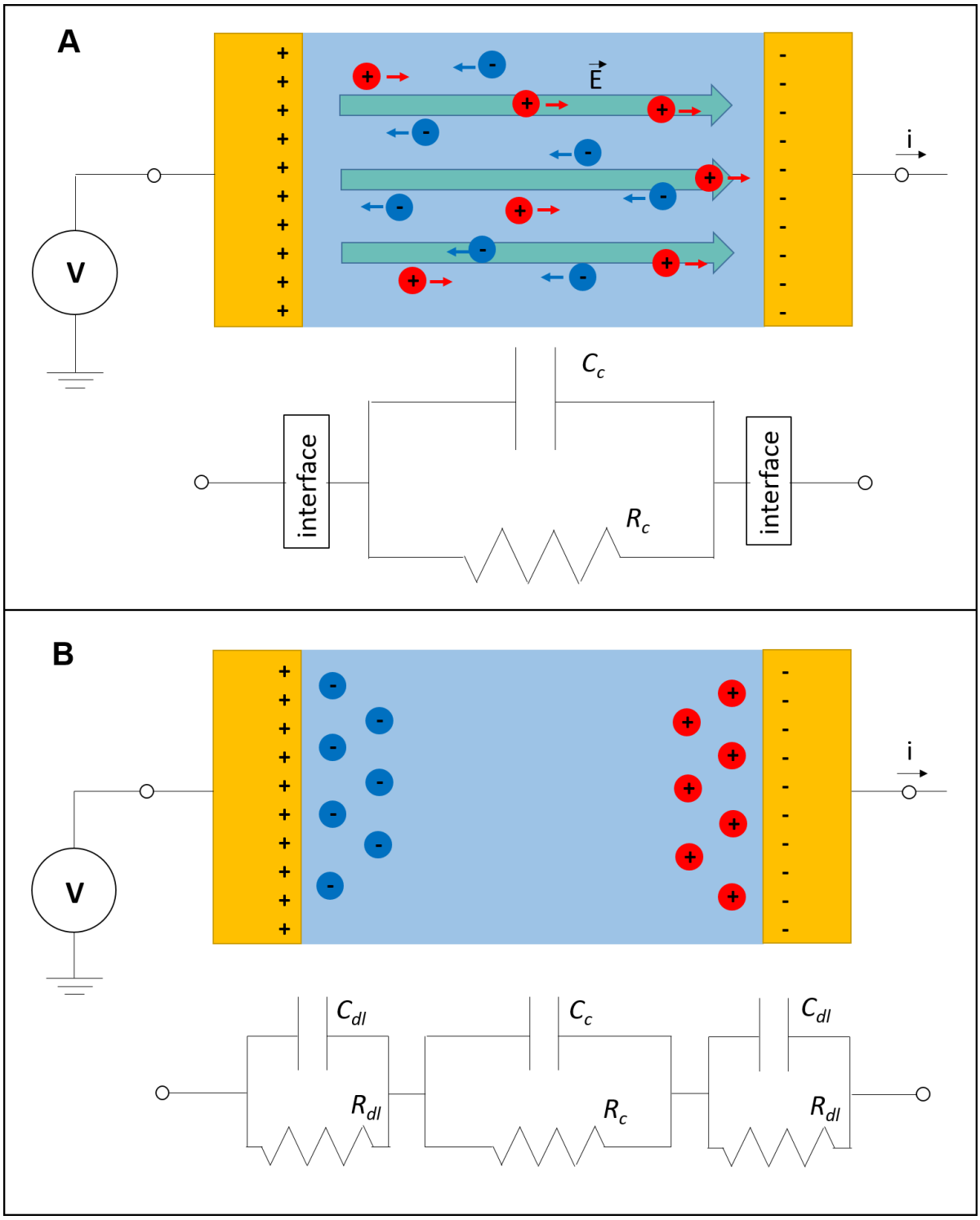

Figure 1.10. Pictorial representation and electrical model of an electrochemical cell with applied voltage.
(A) Turning on the voltage, ions start to move towards the electrodes according to their charge. A capacitance, C_c, and a resistance, R_c, model this behavior. (B) When the ions reach the electrodes, two double layers are formed at the interfaces. Each double layer can be modeled by a capacitance, C_{dl}, and a resistance, R_{dl}.

The resistance and capacitive terms in the electrical models can be estimated by using the fundamental relations:

$$R = \rho \frac{l}{S} \tag{1.16}$$

$$C = \varepsilon \frac{S}{d} \tag{1.17}$$

that take into account materials electrical properties (ρ electrical resistivity, ε dielectric constant) and the geometrical dimensions of each components (l resistance length, S resistance section and capacitance area, d distance between capacitance electrodes).

1.5.4 Cells-device interface: an electrical description

As for a liquid electrochemical cell, an equivalent electrical model can be drawn to describe the interface between an electrogenic cell, like a neuron or a cardiomyocyte, and the sensing metallic electrode where it lies.

In [45], a comprehensive description of the cell-electrode interface is given in the case of a neuron on a planar electrode: it can be also applied in the case of a cardiomyocyte and generalized for nanostructured electrodes. Figure 1.11 shows the equivalent circuit, whose components are described here below.

The system can be described as composed by three components: the cell, the electrode, and the cleft between them. Concerning the cell, the cellular membrane, responsible of APs generation and propagation, can be further divided into two regions: the junctional membrane, that faces the sensing pad, and the non-junctional membrane, that faces the bathing solution and the non-conductive substrate.

Cell and electrode are in very close proximity, separated by a very small gap (the cleft above cited), whose thickness ranges between 10 to 100 nm, as revealed by many SEM studies of cells/electrodes interfaces. The cleft can be modeled by a resistance, usually referred to as the seal resistance R_{seal}, which includes the AP current dispersed at the interface. Higher the resistance, lower the dispersed current and thus higher the electrical coupling between the cell and the electrode. Good values for the sealing resistance are around 1-2 MΩ. A good electrical coupling typically implies a good physical adhesion between the cell and the electrode surface.

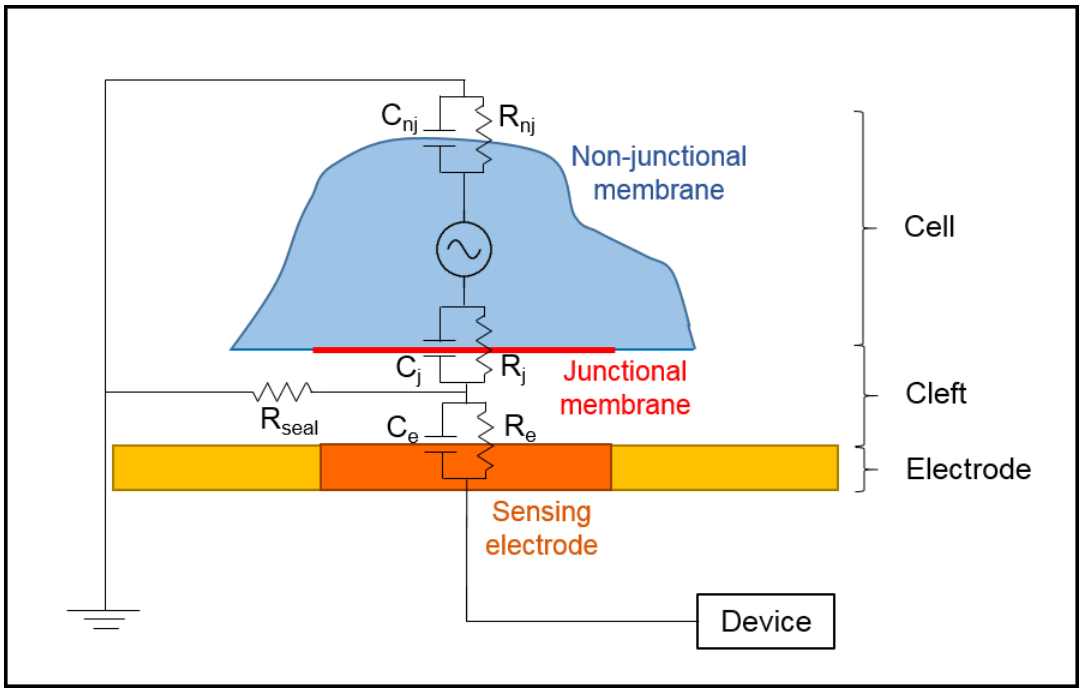

Figure 1.11. Pictorial representation and electrical model of an excitable cell at the interface with a sensing electrode.
The equivalent electrical circuit, superimposed to the pictorial representation, includes all the fundamental components of the system, as described in the main text.

The sensing electrode interface is described by an input impedance, formed by a parallel between a resistance R_e and a capacitance C_e, as in the case of a single electrode in a liquid cell (see section 1.5.3). The capacitance is the dominant term and is attributed to the ion bilayer formed at the electrode surface by the ions normally present in the cellular medium. This capacitive impedance can be decreased by increasing the electrode area: while simply increasing the electrode size decreases the spatial resolution, a more beneficial approach is obtained by increasing the effective surface area in terms of its roughness (by using for example spongy black platinum or porous Ti_3N_4) or by using properly designed 3D nanostructures.

In the same way, the junctional membrane (as well as the non-junctional membrane) can be modeled by a parallel between a resistance R_j and a capacitance C_j (R_{nj} and C_{nj} for the non-junctional membrane). The resistance R_j models the ionic currents that flow across the junctional membrane through the ionic channels or pumps during the AP propagation; on the other hand, the capacitance C_j models the membrane patch that faces the sensing pad.

The approaches described in section 1.4.2, including the penetration of the cellular membrane by patch-clamp or through very sharp 3D nanoelectrodes, as well as by means of induced electro- or optoacustic-poration, aim at achieving a dramatic reduction of the junctional membrane resistance R_j.

Such a modification of the cellular membrane is expected to increase the electrical coupling and thus the measured electrical signal.

2 CHAPTER 2 – MATERIALS AND METHODS

2.1 Electro-Active Zero-Mode Waveguides: fabrication

The EA-ZMWs were fabricated by Focused Ion Beam (FIB) milling of a multilayer structure. The fabrication steps are reported in Figure 2.1 and described in details in the following paragraphs.

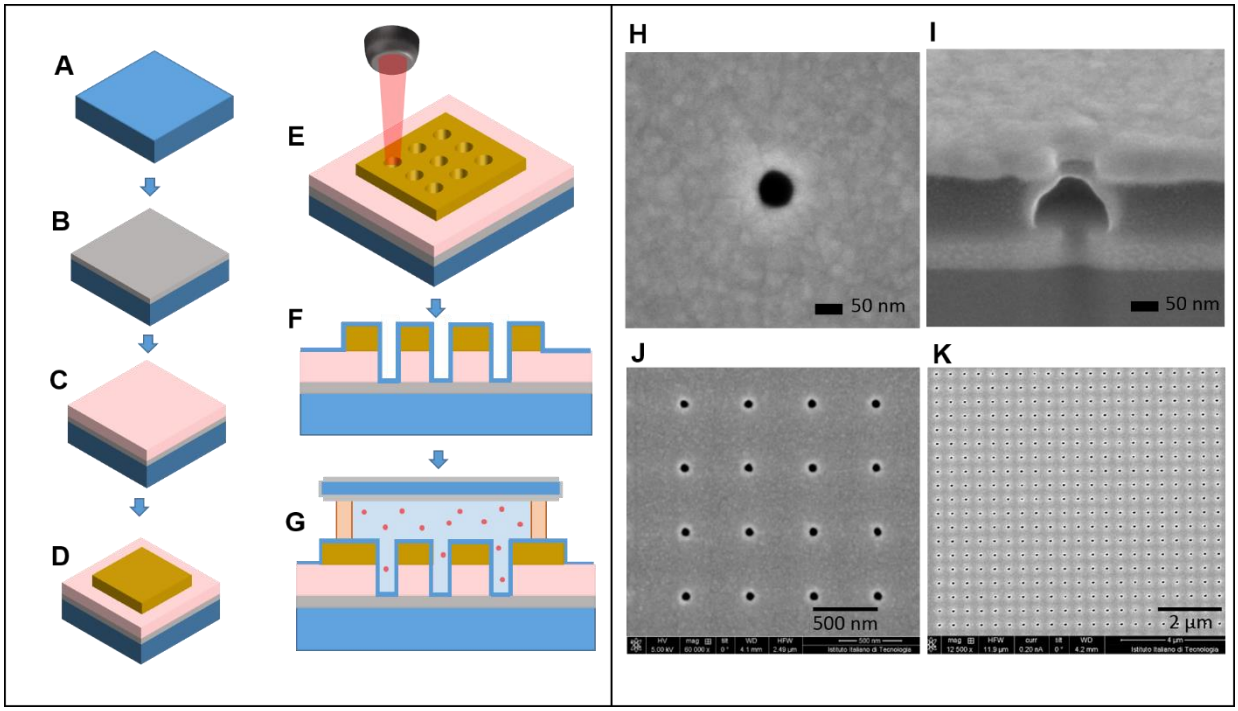

Figure 2.1. Fabrication steps and SEM images of EA-ZMWs device.
Left panel: fabrication steps for EA-ZMWs: A) the device is fabricated starting from a fused silica substrate 2x2 cm^2; B) 100 nm of ITO are deposited by sputtering; C) PMMA A4 (2:1) is spin-coated and baked for a final thickness of 150 nm; D) 100 nm of Au are deposited by sputtering; E) nanoholes are fabricated in the Au and PMMA layers by FIB drilling; F) 5 nm of SiO_2 are deposited by ALD coating; G) a liquid cell is fabricated of top of the nanoholes. Right panel: SEM images of the fabricated nanoholes: top (H) and cross-section (I) view of a single nanohole. (J) and (K): top views of arrays of nanoholes at different magnifications.

Multilayer fabrication

EA-ZMWs devices were built on 2x2 cm^2 fused silica substrates cut from a 10 cm size wafer (University WAFER) by means of a dicer machine (DAD 3220). The substrates were cleaned in a bath of deionized (DI) water with a strong surfactant (Hellmanex III, Hellma Analytics). By sonicating the bath for 5 to 10 minutes, silica particulate matter, originated from the dicing process and redeposited on the substrates surface, was removed. The substrates were then rinsed in DI water

and soaked in acetone for 5 minutes, in order to remove any eventual organic contaminants. Finally, the substrates were washed in isopropanol and dried with a nitrogen flow.

A thick layer of 100 nm of ITO (Indium Tin Oxide) was deposited onto the cleaned substrates by means of RF Ar sputtering (Kenosistec Sputter Coater KS500 Confocal - recipe: 80 W power, 50 sccm Ar flow, 0.5 sccm O_2 flow, room temperature). The obtained ITO layer shows a good tradeoff between transparency and electrical conductance.

A dilution of 950 PMMA A4 resist in A Thinner-anisole (MicroChem) was prepared (2 parts of PMMA A4 and 1 part of anisole) and spin-coated onto the ITO-coated side of the fused silica substrates at 1800 rpm for 60 seconds (Sawatec SM-810-BT). The resist was then baked on a hotplate at 180°C for 5 minutes, increasing gradually the temperature in order to reduce the risk of fractures in the resist layer, induced by high thermal gradients. The finally measured thickness of the PMMA layer was 150 nm (Dektak 150 Profilometer).

Subsequently, a thick layer of gold (100 nm) was deposited by a benchtop sputtering system (Quorum Q150T ES) on an area of 4x4 mm^2 in a central position on the PMMA resist, using a suitably designed stencil mask. The gradual increase of the resist baking temperature and the metal deposition on a small area were foresights adopted to decrease the probability of electrical short-circuits between the gold and the ITO layers, that could decrease the efficiency of the device operation. At this stage of the fabrication, a value for the electrical resistance between the bottom ITO layer and the gold screening layer was measured, by contacting the two films on a probe station, and applying a small bias, around 300 mV. Acceptable values for the electrical resistance can be estimated around 1-10 MΩ.

FIB patterning and ALD coating

Once completed the multilayer structure, nanoholes of circular shape were milled by Ga^+ FIB (Helios NanoLab 650), stopping the beam when the interface between PMMA and ITO was reached. In order to calibrate the process, different milling doses were tested, observing the obtained nanoholes in a cross-section view. A satisfactory result was achieved by milling the substrate with an ionic current of 40 pA and dose of 3.56 $pC/\mu m^2$: the obtained nanoholes have diameter around 60 nm in the gold film layer, that widens to 120 nm in the PMMA layer. Different arrays of nanoholes were fabricated for each sample, with different pitch distances, between 500 nm and 5 μm. After the FIB milling process, the electrical resistance between the gold and the ITO layers was again measured: the FIB drilling could in fact create electrical short-circuits between the two layers. The obtained value was

compared with the one measured before the FIB process: a decrease in the electrical resistance was generally observed down to values of some hundreds of kΩ.

As a final step, the fabricated ZMWs were coated with a thin layer of silicon dioxide (SiO_2, 5 nm) deposited by Atomic Layer Deposition (ALD - FlexAL). This technique allows to obtain a uniform and conformal coating, that turned out to be useful for three main purposes: to protect the PMMA layer from possible degradation induced by the fluorophore solvent; to improve the wettability of the device; to decrease possible fluorophore quenching against the metal components of the device.

Liquid cell fabrication

A small window (3x3 mm^2) was cut in a double sided kapton tape and positioned in correspondence of the gold layer, where the ZMWs were fabricated. After a light oxygen plasma cleaning (Gambetti - recipe: 90 seconds, 100% O_2 gas pressure, 100 W power) performed to increase the wettability of the surface, the obtained cell was filled with the chosen fluorophore dispersion and closed with a microscope glass coverslip coated on both sides with ITO (the two sides are electrically connected). The thickness of the liquid cell can be estimated around 100 μm, i.e. the thickness of the double sided kapton tape. The description of the used fluorophore dispersion is given in Section 2.3.

An electrical wire was connected to the ITO layer of the substrate and another one to the ITO-coated coverslip used to close the liquid cell. These two wires allow to easily connect the device to a function generator when performing the measurements.

2.2 Cells Optical REcording device: fabrication

2.2.1 Top electrode fabrication

The top electrode of the CORE device was fabricated starting from a silicon nitride (Si_3N_4) membrane, a free-standing thin insulating layer, that embodied the interface between the top and the bottom compartments. By FIB milling, arrays of through-nanoholes were fabricated in specific positions on the membrane. These nanoholes were afterwards filled up with gold through galvanic electrodeposition. The latter process also promoted the formation of mushroom shaped microstructures on the counter side of the membrane, which are known to be favorable structures for tight cellular adhesion. As a final step, square shaped gold pads were cut out on the flat side of the membrane by standard optical lithography, in correspondence of the arrays of microstructures.

In the following paragraphs, the fabrication steps are described in more details. They are schematically depicted in Figure 2.2.

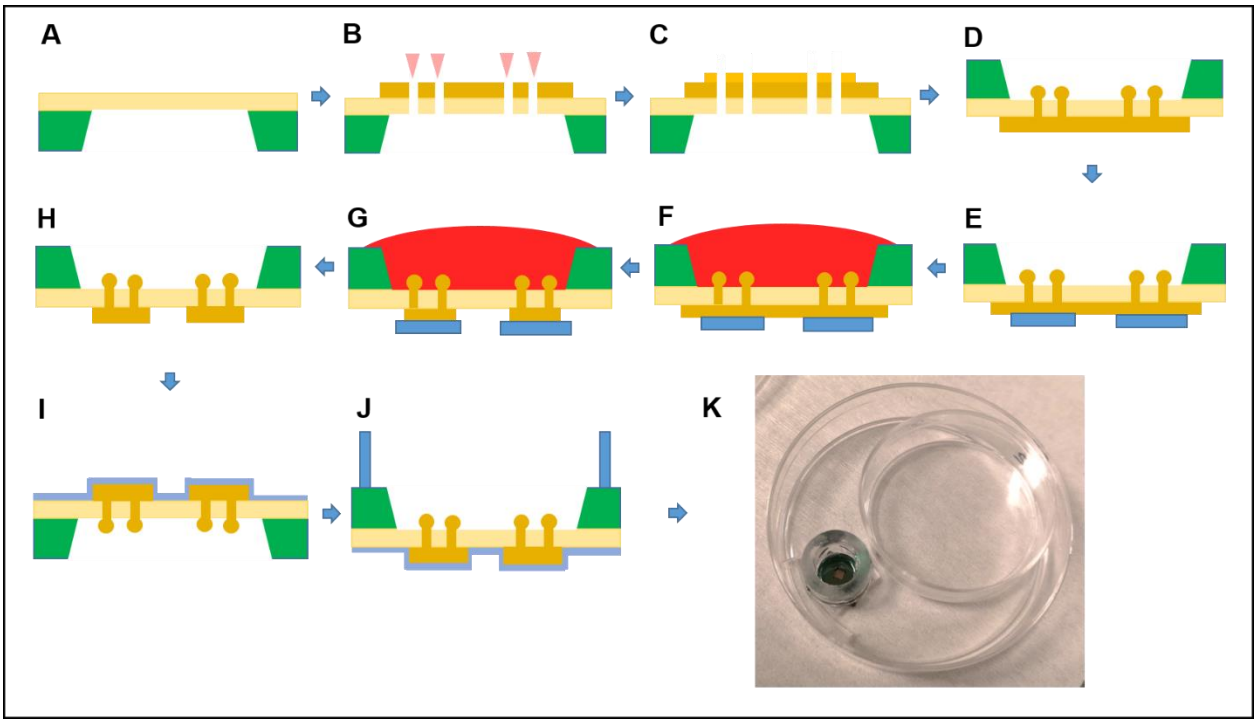

Figure 2.2. Fabrication steps of CORE device top electrode.
Fabrication workflow: A) a 500 nm Si_3N_4 membrane is used as substrate; B) 5 nm of Ti and 20 nm of Au are deposited by e-beam evaporation, and arrays of through-nanoholes are patterned by FIB; C) 20 nm of Au are sputtered on the arrays of nanoholes; D) Au electrochemical growth is performed; E) an optical lithography process is performed on the flat side of the sample; F) a drop of S1813 photoresist is used to protected the gold mushroom-shaped microstructures; G) Au wet etching is performed; H) the photoresists are removed by acetone immersion; I) 3 nm of SiO_2 are deposited by ALD coating; J) a plexiglass ring is positioned to host the cellular culture; K) the sample is packed, ready for the cell culture.

Si_3N_4 membranes fabrication

Silicon nitride membranes were fabricated from a 535 μm thick p-doped Si wafer (100) coated on both sides with a 500 nm thick super low stress Si_3N_4 layer deposited by LPCVD (Low-Pressure Chemical Vapor Deposition) (Silicon Materials).

A layer of a common positive photoresist (MICROPOSIT S1813) was spin-coated onto the wafer at 4000 rpm for 60 seconds and then baked on a hotplate for 5 minutes at temperature T = 95°C. Through a conventional optical lithography process, the resist layer was UV exposed in square-shaped areas and in rectangular-shaped lines (SÜSS MicroTec Mask Aligner), in order to obtain respectively 1.5x1.5 or 2x2 mm^2 membranes and edges to guide the wafer cleavage procedure. Subsequently, resist development was performed by soaking the wafer for 1 minute into the developer solution (MICROPOSIT MF-319 Developer) and then washing it immediately for 1 minute in DI water.

Finally, the wafer was dried with a nitrogen flow and the excess of photoresist was removed by oxygen plasma cleaning (recipe: 120 s, 100% O_2, 100 W).

The exposed Si_3N_4 areas were etched by Reactive Ion Etching (RIE, SENTECH SI500) with trifluoromethane (CHF_3) that selectively remove the silicon nitride layer. Thereafter, the resist mask was removed by immersion in acetone for 5 minutes, followed by washing in isopropanol. Finally, the exposed silicon was wet etched in a solution of 30 wt% potassium hydroxide (KOH) for 8 hours and soaked in mQ water overnight in order to remove any residues of silicon and KOH. The KOH wet etching process removes selectively the silicon from the (100) surface, stopping the process when the (111) surface is exposed. The angle between the two surfaces is equal to 54.74°.

The wafer was cleaved manually along the rectangular-shaped lines above mentioned, obtaining membranes of 1x1 cm^2 or 1.5x1.5 cm^2. The obtained membranes were used as substrates for the subsequent fabrication steps.

FIB patterning

The central region of the membrane flat side was coated with 5 nm of titanium, as adhesion layer, and 20 nm of gold, by e-beam evaporation (Kurt J. Lesker PVD 75). The gold coated side of the membrane was then exposed to the FIB Ga^+ ionic beam and arrays of through-nanoholes were drilled in the whole area of the membrane (current = 0.79 nA, dose = 15.69 pC/μm^2, pitch = 2.5÷3.5 μm). The obtained nanoholes have a conical shape, with diameter of 300 nm on the exposed side and 200 nm on the exit side. The exposed area and the pitch parameter define the nanoholes number and their mutual distance in each array.

Together with the nanoholes, three markers with cross shape were milled just in the gold layer, outside the Si_3N_4 membrane, to be used successively to guide the sample alignment in the optical lithography step.

On the gold coated side of the membrane, where the through-nanoholes were milled, 20 nm of gold were sputtered by a benchtop sputtering system in order to coat the border of the holes that the FIB drilling had uncovered. This step is fundamental in order to promote the successive process of gold galvanic growth inside the nanoholes. In order to leave the markers unaltered, they were protected by a suitable stencil mask during the sputtering process.

Gold electrodeposition

In this step, the through-nanoholes in the membranes were filled with gold, up to complete closure, by galvanic electrodeposition. This process also promoted the formation of mushroom-shaped nano-

/ microstructures on the counter side of the membrane, that are known to be good anchoring sites for cells [46].

In practical terms, each sample was electrically connected to the negative terminal of a power generator and fully immersed, one at a time, into the plating bath, made of a solution of $K[Au(CN)_2]$ dissolved in water (Parador HS, [Au] = 3 g/L, pH = 4.2). A proper counter electrode was connected to the positive terminal and immersed into the plating bath, facing the sample. The electrodeposition was performed by setting a specific current and controlling the time duration of the process itself. In order to be reproducible, the temperature of the bath was kept constant at 40°C by using a hotplate with a thermocouple. Figure 2.3 A and B show SEM images of the gold mushroom-shaped electrodes obtained by setting the current at 35 mA, after 5 minutes of electrodeposition. The diameter of the obtained structures was between 1.3 and 1.6 μm and the height between 600 and 800 nm. The chosen parameters allowed to obtain a rough surface that is considered favorable for cellular adhesion and thus for electrical coupling. As explained in [47], such a surface roughness is an indicator of a fast growth rate process. On the other side of the membrane, the electrodeposition process led to the growth of a thick layer of gold (thickness of 150 nm, Profilometer). After the galvanic growth, the sample was rinsed in water and cleaned by oxygen plasma (recipe: 180 s, 100% O_2, 100 W).

The process of galvanic electrodeposition is very convenient because it can be used at the wafer level, allowing easily to scale up the device production.

Optical lithography

The planar golden side of the membrane was subjected to optical lithography in order to obtain an array of square pads in correspondence of the mushroom-shaped electrodes. The lithography was performed by spin-coating an image reversal photoresist (MicroChemicals AZ5214) after a primer solution (H.M.D.S. TECHNIC) (spin-coating at 4000 rpm for 60s for both the photoresist and the primer) and then baking the sample at 120°C for 1 minute. The primer solution allows to improve the adhesion of the photoresist to the substrate: this step was fundamental in order to avoid the detachment of the exposed resist during the development process.

A suitable mask was designed with arrays of empty square shaped elements. Different arrays with squares of various size and distance have been designed and included in the mask, in order to test several configurations. The chosen lateral sizes of the squares are equal to 10 and 30 μm; the distance between the squares is equal to their lateral size or three times this value.

By relying on markers alignment, the mask's empty squares were aligned onto the FIB-made arrays of nanochannels, filled by gold electrodeposition, and the sample was exposed to UV light for 7 seconds. Thereafter, the photoresist was inverted by a post-exposure bake at 112°C for 2 minutes and a flood UV light exposure of 30 seconds.

The sample was finally developed (MicroChemicals AZ5214 Developer) for 45 seconds and then rinsed in water. The developed sample was examined under an optical microscope equipped with a UV filter, in order to control the stage of development and the correct alignment between the squares and the FIB-made patterns.

Gold etching process

After the optical lithography step, the sample is ready for the gold-etching process that creates the array of gold electrode pads on its planar side (Figure 2.3 C and D).

Before to start with the gold-etching, the sample was exposed to a light oxygen plasma cleaning (recipe: 90 s, 100% O_2, 100 W), in order to remove any residues of resist that could have remained in the developed regions of the samples. Most importantly, the gold nanostructures on the front side of the sample were covered with a drop of photoresist (3 μL of MICROPOSIT S1813, baked at 95°C for 15 minutes) in order to protect the gold nanostructures from the etchant solution.

Each sample was soaked in the gold etchant solution (Merck, gold etchant standard) for 30 seconds and then washed three times in cleaned DI water. The stage of the etching process was controlled under the microscope: in the case of incomplete etching, the process was repeated for a shorter time. Once completed the gold etching process, the resists on both sides of the membrane were removed by immersion of the sample in acetone (5 minutes) and isopropanol (2 minutes). In order to remove any chemical residues of the process, an oxygen plasma cleaning (recipe: 180 s, 100% O_2, 100 W) was finally performed on both sides of the sample.

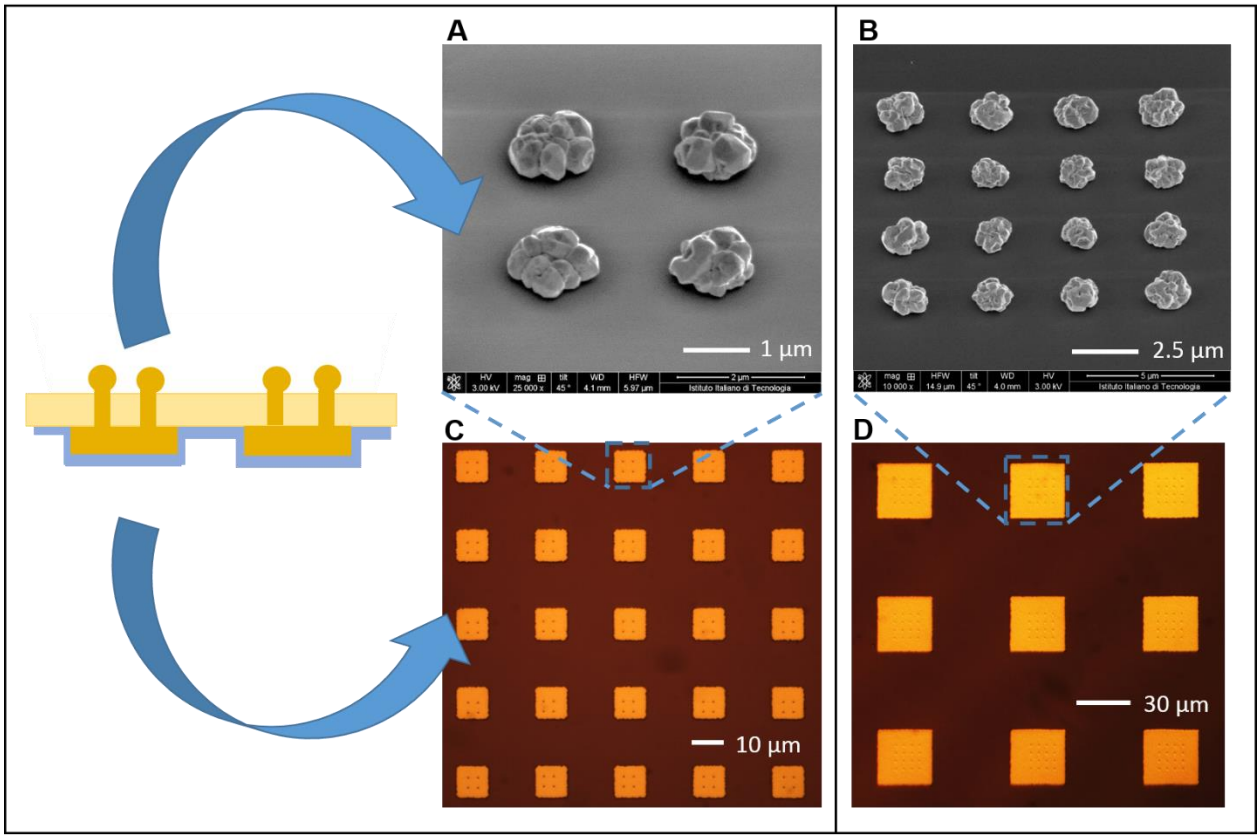

Figure 2.3. SEM and optical images of the CORE device top electrode.
(A) and (B): SEM images of the mushroom-shaped nanostructures. (C) and (D): optical images of two different gold electrodes arrays: (C), electrode pads with size 10 µm and pitch 20 µm; (D), electrode pads with size 30 µm and pitch 60 µm.

Silica coating, ring positioning and sample packaging

The fabrication procedure was completed by depositing a thin uniform layer (3 nm - ALD) of SiO_2 on the back side of the sample, where the gold squared pads were fabricated. The silica layer is expected to increase the wettability of the surface that will be placed in contact with the fluorophore solution, and, moreover, to protect the fluorophore from quenching against the gold electrodes.

A plexiglass ring of internal diameter 8 mm, wall thickness 2 mm, and height 8 mm was cut from a plexiglass tube and smoothed with an abrasive sheet. By using a not cured PDMS preparation (PolyDiMethylSiloxane, Sylgard 184, Dow Corning) as glue paste, the ring was positioned on the front side of the sample and then cured in oven at 65°C for at least 1.5 hours.

As a final step the back side of the sample was treated with oxygen plasma (recipe: 120 s, 100% O_2, 100 W) in order to further clean the surface and improve its wettability. The sample was then placed in a plastic petri dish with diameter 6 cm, where a PDMS spacer allows to keep the membrane lifted up from the petri dish bottom and in a stable position, thanks to its adhesive properties. A smaller

petri dish, of diameter 3.5 cm, was placed inside the 6 cm petri dish, just beside the sample: filled with water, it is expected to limit the culture medium evaporation during the cells incubation process at 37°C.

The samples were then handed to the biologists, in order to start the cellular culture inside the ring, on the nanostructured side of the membrane. Once the cells were active, after 4 to 8 days according to the type of cardiomyocytes, samples were recovered back to be measured.

2.2.2 Bottom electrode fabrication

The bottom electrode was fabricated following the same workflow of the EA-ZMWs device, illustrated in Figure 2.1. For a preliminary test, nanoholes arrays with different pitch, from 150 nm to 800 nm, were fabricated. After having characterized their SNR (see section 4.1.1), the configuration that gave better results was replicated on a large area (approx. 2.5 x 2.5 mm^2), and then used for the experiments with cells.

2.3 Fluorophore solution

The fluorophore used for both the EA-ZMWs and the CORE experiments was Rhodamine 6G (R6G) (Merck). It is commercialized in the form of a salt powder and can be dissolved in water and many organic solvents (methanol, ethanol, isopropanol,…). Depending on solvent pH properties, it can show a positive electrical charge [48].

The chosen solvent to dissolve R6G was ethylene glycol (Merck). Ethylene glycol is a transparent, slightly polar solvent, with higher viscosity than water. It is characterized by a high boiling point (T_b = 197°C) and very low volatility. This last property makes ethylene glycol particularly suitable for the CORE device, because it prevents its evaporation in the open microfluidic cell (see section 2.4).

In Figure 2.4, the molecular structures of R6G and ethylene glycol are represented, together with the absorption and emission spectra of R6G in ethylene glycol, as measured by the laboratory absorption and fluorescence spectrophotometers (Cary 300 and Cary Eclipse, Agilent). R6G dissolved in ethylene glycol shows an absorption maximum at λ = 534 nm and an emission maximum at λ = 561 nm.

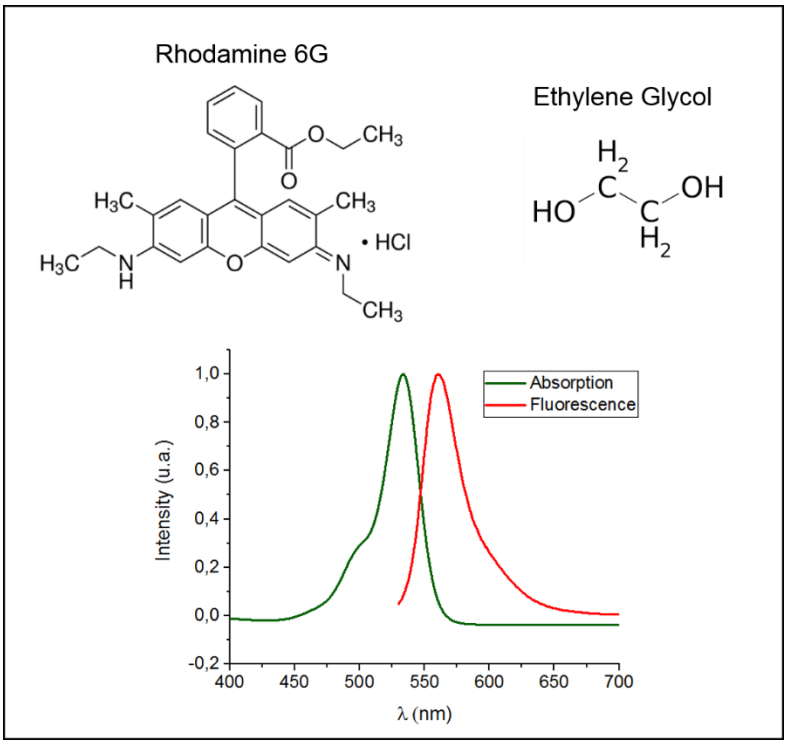

Figure 2.4. Rhodamine 6G fluorophore solution in ethylene glycol.
Molecular structures of rhodamine 6G and ethylene glycol, and measured absorption and fluorescence spectra of R6G in ethylene glycol (R6G concentration = 6.8 μg/mL = 1.4 x10^{-2} mM; excitation wavelength for fluorescence spectrum = 512 nm).

2.4 Measurement setup

The optical setup used is based on an inverted microscope (Nikon Eclipse TE2000-E), that allows to illuminate the sample and collect the emitted fluorescence light from the same objective, placed below the sample stage. The microscope configuration used allows for a widefield illumination.

Device assembling – CORE experiment

In the case of the CORE experiment, the device was assembled directly onto the sample stage: first, the bottom electrode was fixed on the microscope stage by means of two pieces of tapes. After that, a drop of the fluorophore solution (5 μL of R6G in ethylene glycol with concentration 0.14 mg/mL = 0.28 mM) was placed with a micropipette in the center of the bottom electrode surface, where the ZMWs arrays were fabricated. After the drop had spread onto the surface, the top part of the device with the cellular culture, was carefully positioned on the bottom electrode, above the fluorophore solution. An open microfluidic cell was thus realized. This configuration allows to reach a very small spacing between the two electrodes. As a consequence, the electric field generated by the cells APs and acting on the fluorophores is expected to be higher, and thus to increase the device performance.

In order to fix the electrical potential of the two compartments, the ITO layer of the bottom electrode was grounded, and a Pt wire connected to ground was inserted into the cellular medium.

Microscope setup

The optical scheme of the microscope is represented in Figure 2.5. The light source is a mercury arc-lamp that provides a wide excitation spectrum across the visible range. Light, eventually filtered by a neutral density filter in order to limit fluorophore photobleaching, passes through a filter cube set that selects the excitation spectrum, and is afterwards directed through an objective to the device on the microscope stage.

Here, the light excites the fluorophores in solution: the emitted fluorescence light is collected by the same objective, passes through the filter cube set and is finally directed to a CMOS camera (Hamamatsu ORCA Flash 4.0 V3) controlled by a computer (HCImage Live software). The measurements were performed at two magnification levels, with long working distance objectives 20x and 60x (Nikon 20x/0.45, Nikon 60x/0.70). The CMOS camera used has 4 MP, allows for binning up to 4x, has high sensitivity and very fast speed (100 fps on the whole FOV with 4x binning).

The filter cube set adopted is a TRITC filter set (Nikon: λ_{ex} = 543/22 nm, λ_{em} = 591.5/43 nm), whose excitation and emission bands overlap quite well with the corresponding spectra of R6G in ethylene glycol (inset of Figure 2.5).

An halogen lamp on top of the microscope, allows to look at the sample also in transmission mode.

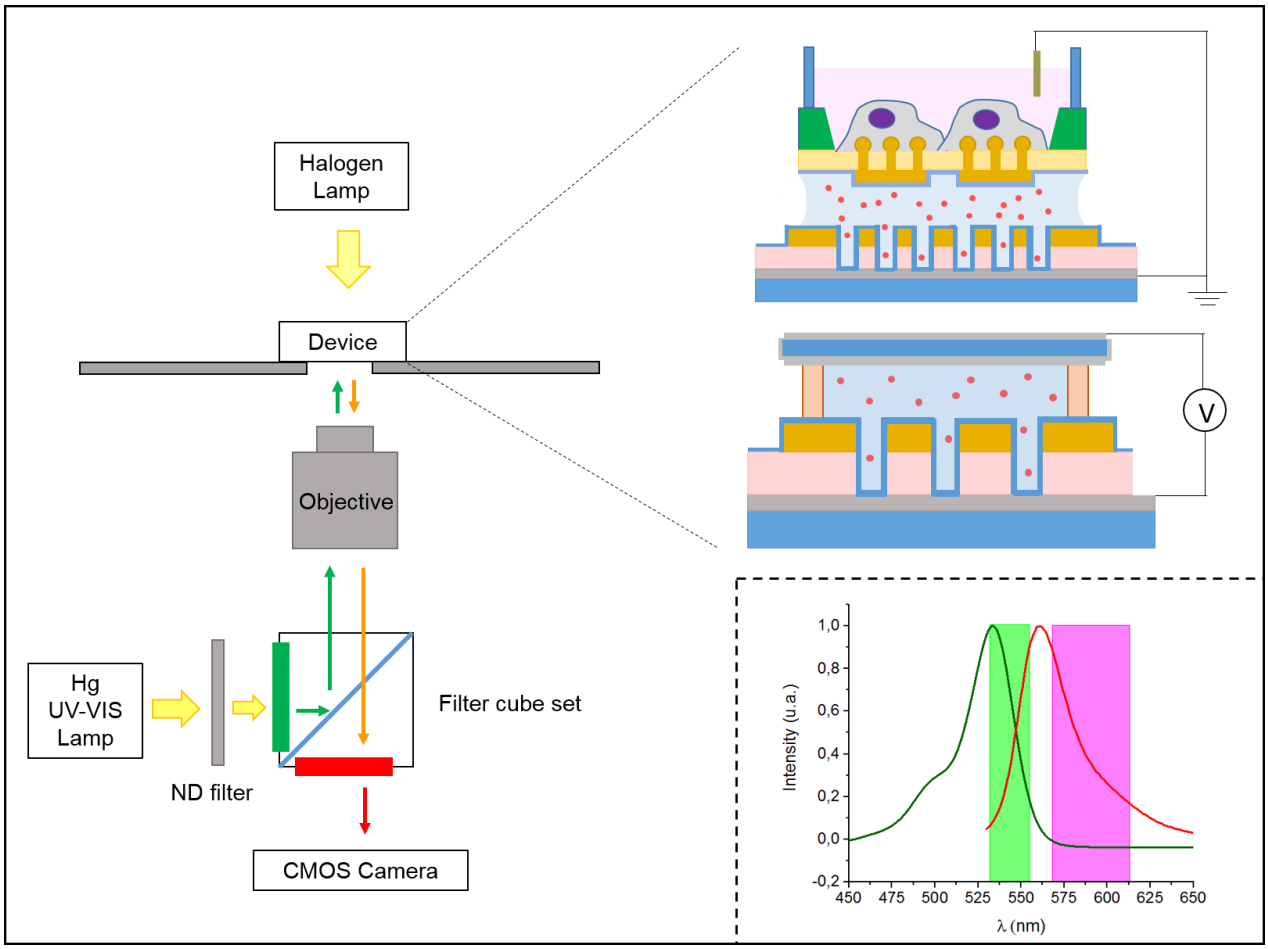

Figure 2.5. Optical setup for EA-ZMWs and CORE experiments.
The optical setup is based on an inverted microscope. In the graph inset, the overlap between the fluorophore absorption and emission spectra and the filter cube set spectra is shown.

2.5 Procedure for data analysis

Video recorded by the CMOS camera were saved in .cxd format (HCImage proprietary file format) and then analyzed with ImageJ 1.52n freeware (U. S. National Institutes of Health, Bethesda, MD). On the first frame of each video, regions of interest (ROIs) were segmented in correspondence of the ZMWs arrays, through the Analyze Particle tool, by setting a proper threshold value for intensity. By using the Multi-measure tool, the mean intensity was calculated for each ROI and for each frame of the video. The output file was saved in .csv format and imported in OriginPro 2016 (OriginLab) for data analysis. The number of frame was converted into the corresponding elapsed time by multiplying it for the inverse of the acquisition frame rate, i.e. the time between two consecutive frames. Finally, the mean intensity of each ROI was plotted with respect to the elapsed time, in order to detect the presence of light signals.

2.6 Human-derived cardiac cells

The cells used for the CORE experiments were cardiomyocytes obtained by differentiation of human-induced Pluripotent Stem Cells (hi-PSCs) [49]. Hi-PSCs are cells generated reprogramming human adult somatic cells by a set of transcription factors and can be differentiated into a variety of cell lineages. Thanks to these properties, they gained in the last two decades lots of attention, both as new model for biomedical research and as new tool for personalized regenerative medicine [50]. Since their discovery, they have been used for studying early developmental processes, to model human diseases in a dish, thereby enabling the identification of new diagnostic markers and potential new drug targets, and to perform large-scale toxicity and drug screens, upon differentiation into appropriate cell types [51]. Hi-PSCs could also be used to directly treat a particular condition of the donor through cellular replacement therapy, by transplantation of genetically corrected autologous cells.

In the cardiology field, hi-PSC lines were established from healthy individuals, and from patients inflicted with acquired (heart failure) and inherited cardiac disorders. Corresponding hi-PSC derived cardiomyocytes (hi-PSC-CMs) were shown to recapitulate in culture the phenotypic characteristics and electrophysiological profiles of native human cardiac cells, and the disease phenotypes of unhealthy patients. Remarkably, hi-PSC-CMs are able to form a beating syncytium, where cells are connected both electrically and mechanically, which behaves similarly to native cardiomyocytes in the cardiac tissue [49].

In the experiments performed and reported in this thesis, the cell lines used were Cor.4U and Pluricyte hi-PSC-CMs from Ncardia.

3 CHAPTER 3 – EA-ZMWs: RESULTS AND DISCUSSION

3.1 Electro-Active Zero-Mode Waveguides

On the fluorescence optical microscope, EA-ZMWs appear as small bright spots as shown in Figure 3.1 B: the detected light comes from the fluorophore molecules that flow inside the nanoholes and are excited by the incident light (R6G concentration in ethylene glycol = 0.14 mg/mL = 0.28 mM) (Figure 3.1 A). On the other hand, fluorophores outside the nanoholes are screened by the thick gold layer, which reflects the incoming light. Some nanoholes are not brighter than the background: probably they are not filled with the fluorophore dispersion, due to possible fabrication failures.

For pitch equal or larger than 800 nm, nanoholes are clearly distinguishable (Figure 3.1 B2, B3, B4), and analysis on single EA-ZMWs can be performed. In order to analyze the behavior of a single EA-ZMW, avoiding any interference from neighboring nanoholes, EA-ZMWs with pitch equal to 5 μm were fabricated for the experimental measurements.

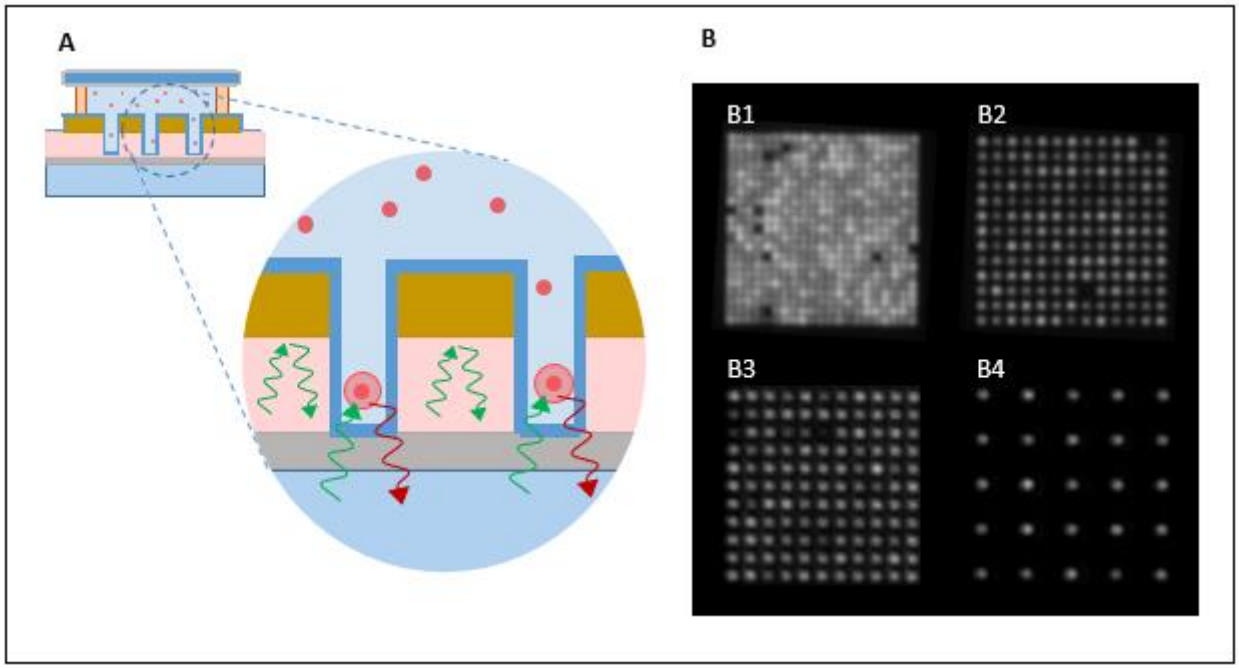

Figure 3.1. EA-ZMWs filled with R6G solution in ethylene glycol.
Schematic picture (A) and captured images (B) of EA-ZMWs with different pitch: B1) 0.5 μm; B2) 0.8 μm; B3) 1 μm; B4) 2.5 μm.

3.1.1 Tuning fluorophore concentration

In order to test if it is possible to tune fluorophore concentration inside the EA-ZMWs, a voltage step function was applied to the system. In particular, with the goal to decrease fluorophore concentration down to, in principle, the single-molecule level, a series of "negative" voltage steps were chosen (3 steps of -500 mV and time duration 30 s, see Figure 3.2 A). In this case, the top electrode was grounded and the bottom ITO electrode was connected to the positive pole of the wave function generator. Since R6G dissolved in ethylene glycol has a positive electrical charge, this sequence of voltage steps is expected to push R6G molecules out of the nanoholes.

As shown in Figure 3.2 B, the light intensity integrated on the EA-ZMWs decreases by steps, following the shape of the applied electrical voltage. These intensity variations can be related to corresponding variations of R6G concentration inside the nanoholes. In a simple picture that ignores photobleaching effects (in a first approximation, because counterbalanced by molecules diffusion in-and-out the nanoholes), the EA-ZMW mean light intensity, corrected for light background, can be considered proportional to the fluorophore concentration inside the nanoholes. For every voltage step of -500 mV, light intensity decreases approximately of 50 counts, which correspond to a 12% decrease of the EA-ZMW mean light intensity. After the three steps, light intensity has decreased of around 36%: according to the simple model above described, fluorophore concentration has decreased by the same amount.

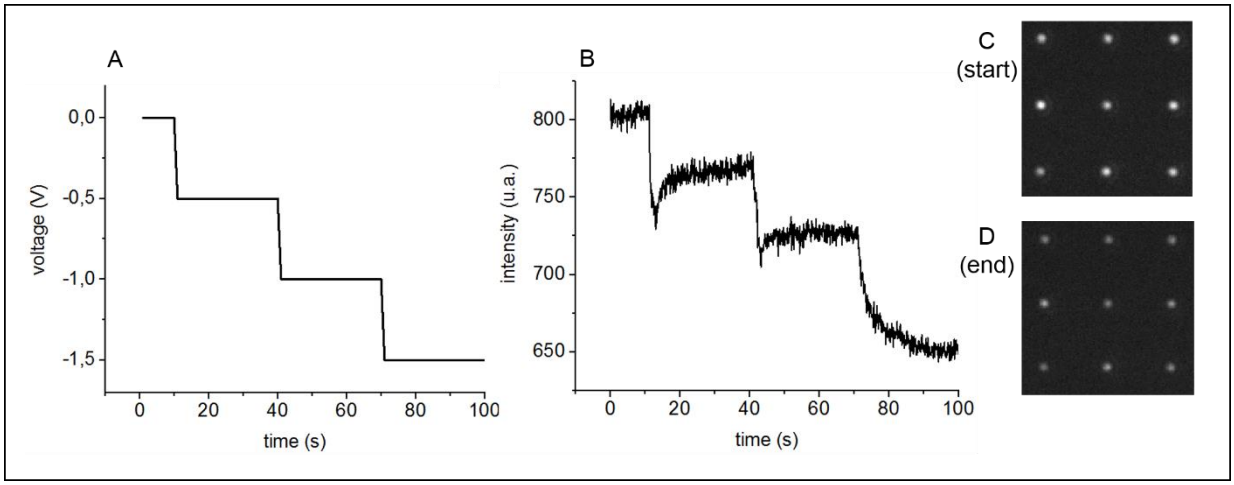

Figure 3.2. Tuning fluorophore concentration in EA-ZMWs.
By applying a series of "negative" voltage steps (A), mean light intensity integrated from a single EA-ZMW varies accordingly (B). The decrease in fluorescence light intensity can be appreciated also in the microscope images reported on the right, relative to the starting (C) and ending (D) points of the experiment.

3.1.2 Controlling fluorophore residence time

By applying voltage pulses of different time duration, the possibility to control fluorophore residence time inside the EA-ZMWs was studied. The applied voltage consisted of square "positive" pulses of amplitude 1V: in this case, the bottom ITO electrode was grounded and the top electrode connected to the positive pole of the wave function generator. These positive pulses are expected to drive the positively charged fluorophores inside the nanoholes, and thus increase the emitted light intensity.

In Figure 3.3, the results for light intensity variations, measured while applying voltage square pulses of amplitude 1 V and time durations 1 s, 500 ms, and 150 ms, are shown. Light intensity results to follow quite faithfully the applied voltage (compare Figure 3.3 (A) and (B)): the increase in light intensity can be explained by fluorophore electrically-driven motion inside the nanoholes, while light decrease by fluorophore diffusion motion outside the nanoholes. Both these light variations are fast (they are clearly detectable for electrical pulses as short as 150 ms), as a consequence of the very small size of the optically active volume where molecules are "visible", that can be estimated roughly equal to the nanohole volume below the gold screening layer (see Figure 3.1 A).

Starting from known values of diffusion and electrical mobility of a chemical species in a specific solvent, the corresponding quantities for R6G molecules dissolved in ethylene glycol can be derived, by using equations 1.2 and 1.8.

Diffusion coefficient *D* of R6G in water at 25°C is equal to $4 \cdot 10^{-6}$ cm^2/s, as reported in literature [52]. By correcting this value for ethylene glycol viscosity (ethylene glycol viscosity = 16.2 mPa·s; water viscosity = 0.89 mPa·s), *D* of R6G in ethylene glycol can be estimated equal to $2.2 \cdot 10^{-7}$ cm^2/s.

In the case of electrical mobility μ, starting from a well characterized species (as an example, Na^+ with $\mu = 5.19 \cdot 10^{-4}$ cm^2/Vs in water at 25°C [42]), it is possible to estimate the electrical mobility of R6G in ethylene glycol, by correcting for the ionic hydrodynamic radius *r* ($r_{Na^+} = 102$ pm; $r_{R6G} = 770$ pm – values calculated from diffusion coefficients in water and approximated valid also for ethylene glycol) and again for the viscosity of the solvent. In this way, the electrical mobility of R6G in ethylene glycol can be computed equal to $\mu = 3.6 \cdot 10^{-6}$ cm^2/Vs.

For voltage pulses of 1 V, an electric field equal to $E = 10^4$ V/m can be estimated between the electrodes, according to equation E = V/d (electrodes distance d = 100 μm); a generated drift velocity $v_D = 3.6 \cdot 10^{-6}$ m/s can be afterwards computed (equation 1.7). With this velocity, molecules can cover the whole vertical distance of the nanoholes volume (150 nm) in around 40 ms, a time value compatible with the fast increase of light intensity shown in Figure 3.3 B-B1-C-D.

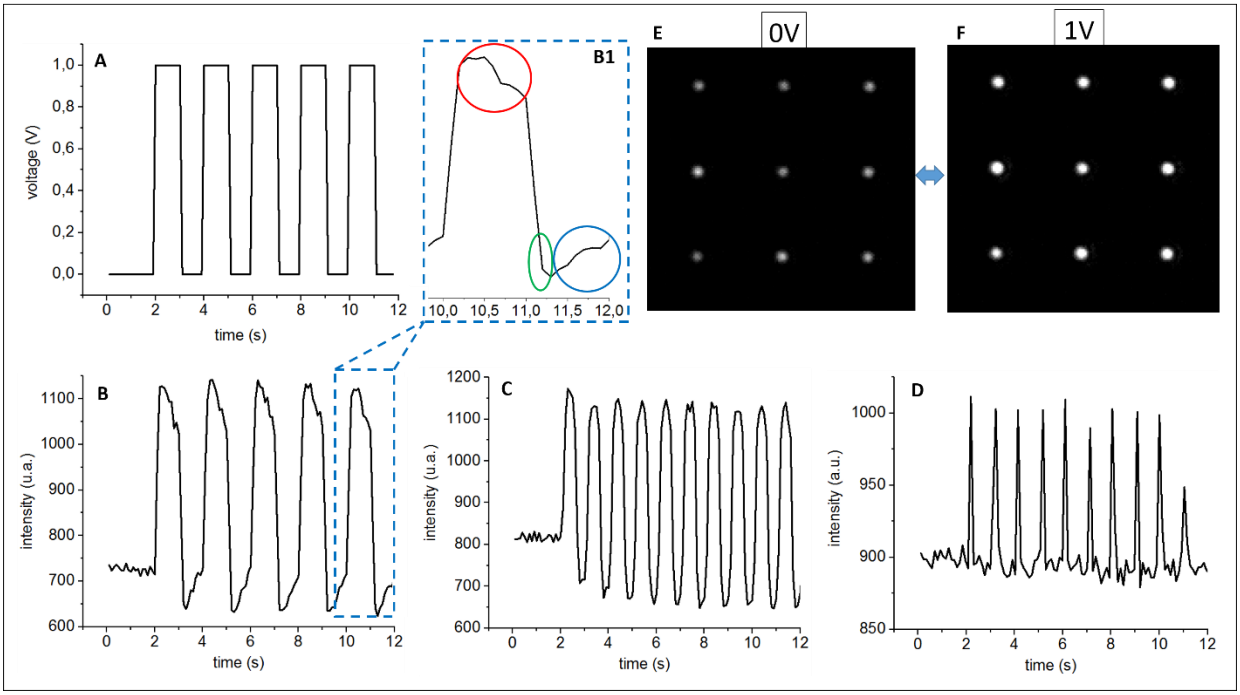

Figure 3.3. Controlling fluorophore residence time in EA-ZMWs.
(A) Applied square voltage pulses with amplitude 1 V and time duration t = 1 s. (B-C-D) Light intensity recorded from a single EA-ZMW, while applying voltage pulses of time duration t = 1 s (B), t = 500 ms (C), t = 150 ms (D). (B1) Zoomed light pulse with highlighted features, as explained in the main text. (E-F) Optical images of the EA-ZMWs when pulses are OFF (E) and ON (F): when pulses are ON, EA-ZMWs are brighter (pictures relative to graph (B)).

When the voltage pulse turns off, R6G molecules diffuse out of the nanoholes. As a rough estimate of the time scale involved, starting from the calculated diffusion coefficient for R6G molecules in ethylene glycol, a mean square distance equal to the square of half the vertical height of the nanoholes is covered in around 400 ms (equation 1.1). This value is larger than the duration of light intensity decrease, reasonably because it does not include the contribution due to molecules concentration gradient (fluorophore concentration has increased in the nanoholes during pulse application with respect to the bulk of the solution - see equations 1.3 and 1.4) and the effect of the electrostatic repulsion between R6G molecules.

The features highlighted by circles in Figure 3.3 B1 are probably due to capacitive effects that arise in the liquid cell during the application of a voltage pulse, and involve: molecules diffusion out of the nanoholes (red circle), molecules over diffusion after pulse switching-off (green circle), molecules re-diffusion inside the nanoholes (blue circle). The fluorescence decrease while the pulse is switched-on (red circle) can also be due to the increased photobleaching effect on fluorophore molecules held inside the nanoholes by the electric field. As an additional note, the particle re-diffusion time scale

(blue circle) is much more compatible with the time value of 400 ms above computed for free-diffusion: in this phase, effects of molecules concentration gradients and electrical repulsion should be less relevant with respect to the pulse switching-off phase.

Finally, by changing fluorophore solvent, passing for example to isopropanol or water (isopropanol viscosity = 2.1 mPa·s; water viscosity = 0.89 mPa·s), both the electrophoretic and diffusion dynamics should become faster, and the device should become able to work also for pulses with shorter time duration. In fact, by decreasing the solvent viscosity, both the electrical mobility and the diffusion coefficient increase, as expressed by equations 1.2 and 1.8. As a consequence of the increase of the electrical mobility, the drift velocity increases as well (see equation 1.7), and therefore the electrophoretic dynamics becomes faster. Concerning the diffusion motion, when the diffusion coefficient increases, the time needed by a molecule to diffuse out of the volume of a single ZMW is expected to decrease, as expressed by equations 1.1 and 1.3.

4 CHAPTER 4 – CORE DEVICE: RESULTS AND DISCUSSION

4.1 Cells Optical REcording device

In this chapter, the results obtained for the CORE device will be presented and discussed. In the first section, a preliminary study with an applied external voltage, performed to define the best configuration for the ZMWs arrays on the bottom electrode, will be described. Successively, a characterization of the device functioning, performed by applying external voltage pulses that emulate cellular APs, will be shown. Finally, the experimental results of the measurements on cells will be presented and extensively discussed. Both the measurements with the external voltage source and the cells were performed using top electrode with pads of size 30 μm and pitch 60 μm.

4.1.1 Study of bottom electrode ZMWs configuration

In order to increase the optical signal coming from the ZMWs on the bottom electrode, dense arrays of ZMWs were fabricated. By summing up ZMWs signals, device sensitivity for an applied voltage is expected to increase, and possibly to enable the detection of very small voltage pulses, like cellular APs.

In order to find the best configuration for bottom electrode ZMWs, different ZWMs arrays with different pitch were fabricated. The arrays have all square shape and lateral size 10 μm, while the pitch ranges from 150 to 800 nm (Figure 4.1 B). A drop of the fluorophore solution was placed on the sample where the arrays were fabricated, and the system was closed with a glass coverslip coated on both sides with ITO (Figure 4.1 A). By focusing alternately on the ZMWs arrays and small scratches made on purpose at a corner of the ITO-coated glass coverslip, the gap distance between the two electrodes was estimated to be approx. 5 μm. By contacting the ITO layer of the bottom electrode, and the top ITO layer of the glass coverslip, by means of a flexible electrical wire moved by a micromanipulator, the optical signals emitted from the different ZMWs arrays in response to an applied voltage were measured. As for example, the inset of Figure 4.1 C reports the optical signals measured by integrating the light intensity on the whole array with pitch 300 nm, after the application of voltage pulses with amplitude 150 mV and time duration 150 ms: clear pulses emerge, with very high SNR. By performing this study on all the fabricated arrays, the SNR was calculated for each configuration of ZMWs, and then plotted with respect to the surface nanoholes density (Figure 4.1 C). Starting from low density values, i.e. few number of nanoholes per unit area, SNR increases with the nanoholes density and reaches a maximum for the ZMWs array with pitch 300 nm. Further increasing the nanoholes density does not improve the sensitivity of the ZMWs array, probably

because of structural instabilities in the nanoholes arrays: as shown in the SEM cross-section image of Figure 2.1 I, nanoholes have diameter that widens to 120 nm in the PMMA layer. If the nanoholes are too much packed, their structure could become less stable, compromising device functioning.

Considering the results of this analysis, the array configuration with pitch 300 nm was chosen for the ZMWs on the bottom electrode. Arrays of nanoholes with square shape, lateral size 10 µm and pitch 300 nm were fabricated on a large area (approx. 2.5 x 2.5 mm^2) of the bottom electrode, separated by distances equal to 30 µm. The covered area is slightly larger than the area of the top electrode with the passing-through contacts, in order to facilitate the alignment between the region of the bottom electrode with the ZMWs arrays and the region of the top electrode with the square pads contacts, during device assembling procedure.

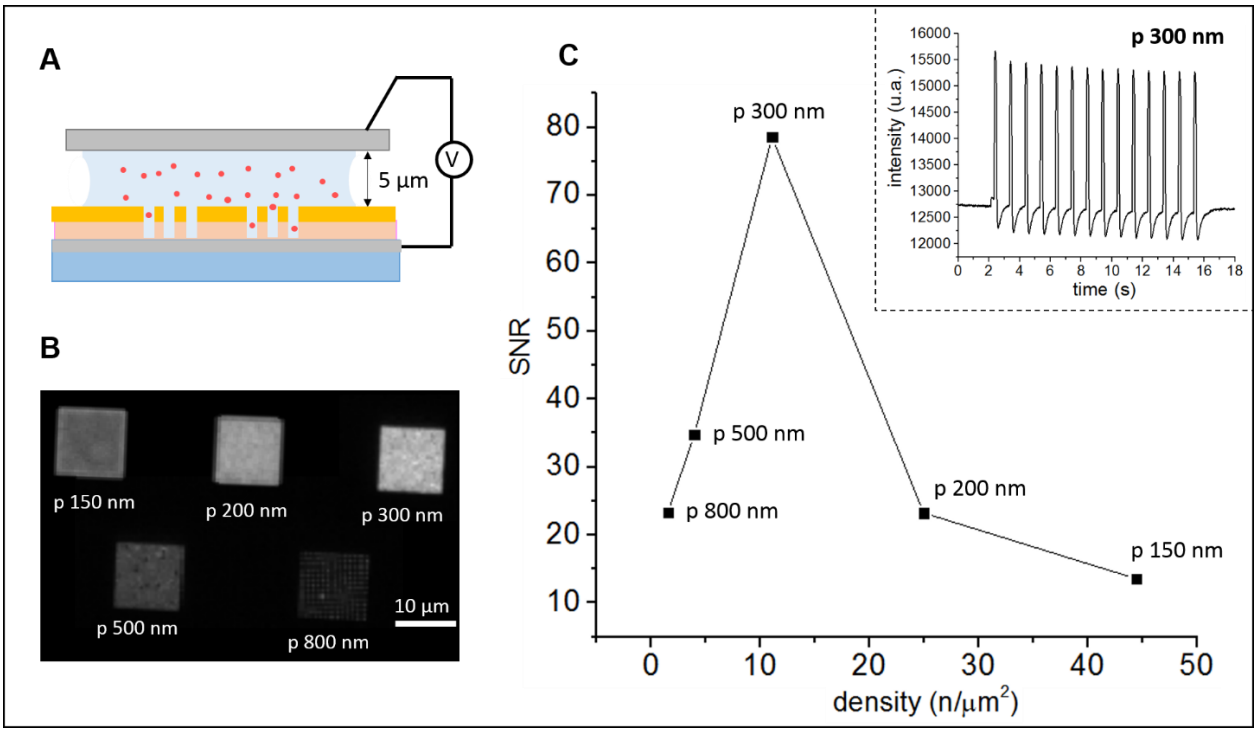

Figure 4.1. Study of the best ZMWs configuration for CORE bottom electrode. (A) Schematics of the measured device. (B) Different arrays of ZMWs were fabricated on the bottom electrode with different pitch *p*. Once filled by the fluorophore solution they appear as bright square. (C) In the inset, optical signal integrated on the whole ZMWs array with pitch 300 nm, after the application of voltage pulses with amplitude 150 mV and time duration 150 ms. In the main graph, signal-to-noise ratio of the optical signals measured on the different arrays studied: the configuration with higher sensitivity to the applied voltage is the one with pitch 300 nm.

4.1.2 Measurements with external voltage

Aim of this study is to verify if the CORE device can record optical signals in response to voltage pulses compatible with cellular APs. In order to easily contact the mushroom-shaped electrodes on the very fragile Si_3N_4 membrane, these electrodes were short-circuited by gold sputter coating (30 nm - benchtop sputtering system Quorum Q150T ES), and contacted by a flexible electrical wire on the membrane thick silicon frame (see Figure 4.2 A).

By turning on the halogen lamp on top of the microscope, the overlap between the ZMWs arrays on the bottom electrode and the square pads on the top electrode was evaluated (see Figure 4.2 B2). In this optical configuration, by focusing alternately on the ZMWs arrays and the square pads, the gap distance between the top and the bottom electrodes was estimated to be approx. 5 μm.

The applied voltage was intended to emulate the cellular APs. As thus, trains of square pulses with amplitude and time duration comparable with the corresponding values of cellular APs (Figure 1.6) and their typically recorded electrical signals (Figure 1.7) were applied. The optical signals, recorded from the ZMWs array of Figure 4.2 B1 that overlaps quite well with a square pad of the top electrode (Figure 4.2 B2), are reported in Figure 4.2 C.

For voltage pulses with time duration 150 ms, a value compatible with the intracellular APs (see Figure 1.7 A), clear optical signals were detected for voltage amplitudes down to 10 mV. By reducing the pulses time duration, in order to get closer to the cellular field potentials (see Figure 1.7 B), optical signals were detected for time duration and voltage amplitude down to, respectively, 10 ms and 10 mV. These values are quite larger with respect to the corresponding values of typically recorded field potentials, of the order of few ms for time duration and few hundreds of μV, up to very few mV, for amplitude.

As a conclusion, the device sensitivity to an external voltage is compatible with the typical values of intracellular APs. However, the detection of field potentials with the CORE device could be challenging.

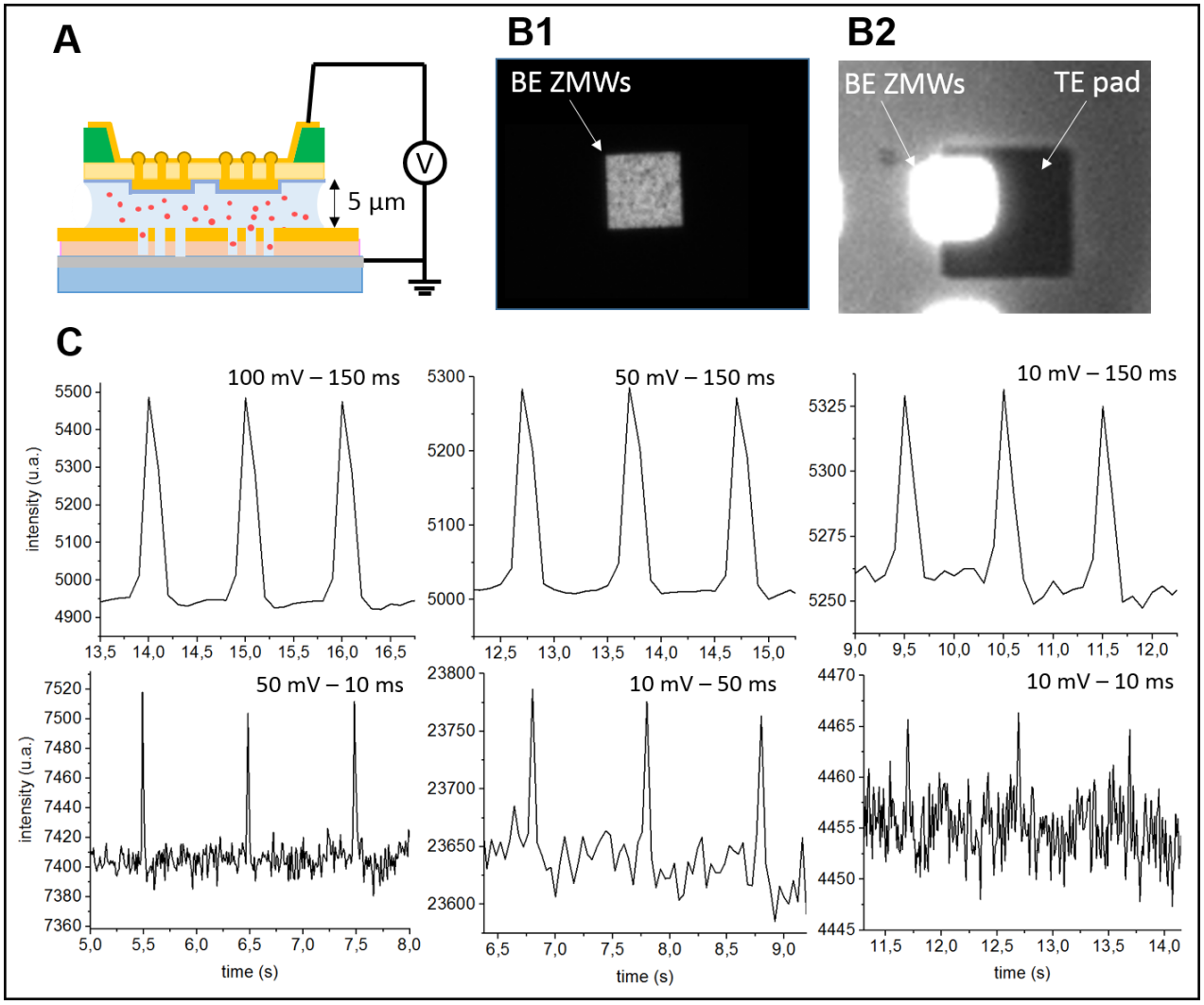

Figure 4.2. Measurements of CORE device with external voltage.
(A) Schematic representation of the CORE device with the applied external voltage. (B1) Bottom electrode ZMWs array with pitch 300 nm. (B2) Same ZMWs array of panel B1 observed by turning on also the halogen lamp on top of the microscope: the square pad of the top electrode is also visible. (C) Optical signals measured in the ZMWs array of panel B1 by applying trains of voltage pulses with different amplitude and time duration (values for amplitude and time duration are specified in each graph). Camera exposure time was set conveniently according to the time resolution needed to detect the pulse train applied. The different SNR between the graphs depends on the different exposure time used for the optical measurement.

4.1.3 Measurements with cells

The cells were cultured on the top electrodes and incubated for several days until they acquired spontaneous beating. The day of the measurement, the sample with cells was taken from the incubator and placed immediately on the bottom electrode, which had been previously fixed on the microscope stage and wet by a drop of the fluorophore solution (see section 2.4). Thereafter, the top electrode pads were aligned with the bottom electrode ZMWs arrays. This procedure was performed by turning

on both the Hg lamp and the halogen lamp on top of the microscope. While the Hg lamp for fluorescence measurements excite the fluorophore molecules filling the ZMWs arrays of the bottom electrode, halogen lamp transmitted light allows to see the top electrodes where the cultured cells lie. By moving carefully the top electrode, a precise alignment of the top electrode pads with the bottom electrodes ZMWs arrays could be achieved (see Figure 4.3 A).

This view modality allows also to see the cellular culture and to monitor cells beating activity. By moving manually the sample stage, it is possible to explore the cells distribution on the device, and therefore study all the different regions of the cellular culture.

Once decided the region to study, the microscope top light was turned off, and video recordings were performed by illuminating the device only from below, in a purely fluorescence microscopy configuration (see Figure 4.3 B). In this view modality, the camera is sensitive only to the fluorophore signal coming from the ZMWs (see section 3.1 for the EA-ZMWs device), avoiding any disturbance from other image elements (in particular, cells boundaries that move during contraction, changing the detected light intensity in close proximity of the ZMWs arrays). Videos were recorded with different frame speeds and for different time courses, in order to be sensitive to all the signals typically recorded from cardiomyocytes by conventional electrical recording methods (see Figure 1.7). In particular, in order to enhance the SNR, the binning option was set to its maximum value, i.e. 4x. The exposure times used were 100 ms, 40 ms, 10 ms, and 5 ms (the last option with FOV reduced at half the full width).

In the following, fluorescence signal measurements will be displayed together with the images of the recorded ZMWs arrays. Images where also the cellular culture and the top electrode pads are visible will be moreover provided, in order to show the cells population on the investigated region, and the overlap between the top electrode pads and the ZMWs arrays.

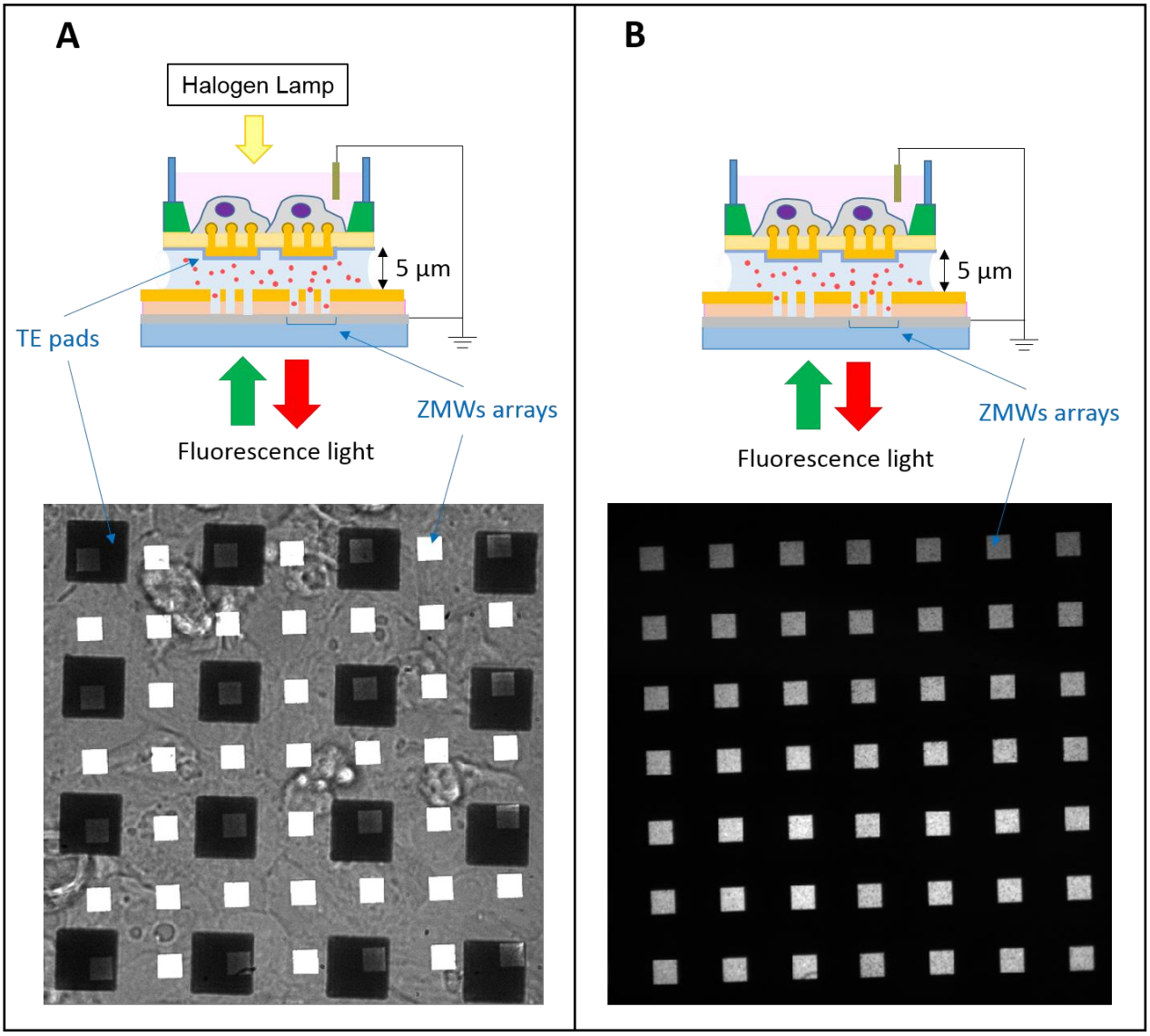

Figure 4.3. Two view modalities for CORE device.
(A) By turning on the halogen lamp on top of the microscope, cells culture and top electrode pads can be made visible. A precise alignment between the top electrodes pads and the bottom ZMWs arrays can be achieved. (B) When performing cellular optical recording, the top light was turned off, in order to be sensitive only to the fluorescent signal of the ZMWs arrays. (Images obtained with 60x magnification).

Action potentials measurements

The typical measurement session on one sample lasted for about 2-3 hours. In each experimental session, several videos were recorded from different parts of the cell culture. The videos were not analyzed in real time but saved for later analysis.

The results reported in this section refer to three different samples, where the cells were well distributed on the top electrode and exhibited spontaneous contractile activity. When performing

video analysis, a background image was subtracted to each frame, in order to highlight any light intensity variation in the recorded region. This procedure was not performed during video recording because resource demanding, and producing a significant slowdown of the frame speed.

After background subtraction, some ZMWs arrays are observed to blink, as shown in the zoomed array of Figure 4.4 C1 and C2: light emitted from the ZMWs undergoes clearly to an increase on the whole array area. By integrating the fluorescence light intensity on the whole ZMWs array, optical signals clearly emerge with very regular shape, constant repetition rate and high SNR (Figure 4.4 D). Remarkably, the periodicity of these optical signals, around 1 pulse every 8 seconds, is the same of the cells contraction, as documented by video recording where the cellular culture is also visible.

At this point, the following observations can be made. First, remembering that cells contraction and APs firing are intimately coupled and occur at the same time (see section 1.4.1), the periodicity of the measured optical signals is therefore the same of the cells APs. Second, the optical signals shape is compatible with the ones for APs, in particular with the ones depicted in Figure 1.6 and Figure 1.7 A. Therefore, by relying on the operation principle described in Figure 1.8, these light pulses can be associated to the electrical activity of the cellular culture, and, more precisely, to the cells AP pulses. The cell AP, upon polarization of the electrode where the cell lie, is believed to push fluorophore molecules in the ZMWs nanoholes, producing an increase of the light optical signal. When the AP ceases, fluorophore molecules are expected to diffuse out of the nanoholes, rebalancing their concentration and re-establishing the ZMWs resting fluorescence light intensity.

The light signals associated to cells APs have shape and time duration that are much more similar to those of intracellular APs than those of field potentials (see Figure 1.7). In the framework of microelectrode recording, this observation can be quite troublesome to explain: in fact, it is very unlikely that the mushroom-shaped microstructures performed spontaneous poration, since they have no surface features considered sharp enough to promote this process [53]. Moreover, no light or electrical stimuli were applied during the measurements in order to porate the cellular membrane. In our opinion, this observation can be explained considering that the electrodes where the cells lie are floating electrodes, as opposed to microelectrode technology where they are fixed to known potentials. Due to their floating nature, these electrodes are believed to assume the actual membrane potential of the cells, which corresponds to the intracellular AP (Figure 1.7 A).

Besides this comment, it has to be noticed that the time duration of the recorded light pulses (around 1.5 s at the 50% of AP amplitude) is slightly larger than the typical time duration of cardiomyocytes APs. This can be possibly due to a slowdown of the cellular activity, confirmed also by a decrease of

the beating rate with respect to physiological values: for this sample, cells were exhibiting around 1 pulse every 8 seconds, a frequency much lower than typical beating rate (1 pulse every second). The slowdown of cellular activity can be caused by the external environment where the cells lie, which is clearly different from their biological environments. Moreover, while cells physiological temperature is 37°C, my experiments were performed at room temperature, and the lowering of the environmental temperature is known to decrease cellular activity. Finally, another explanation of the longer duration of AP light pulses, could be ascribed to the fluorophore dynamics, which occurs with longer time constants, with respect to electrons dynamics in more conventional electrical recording methods.

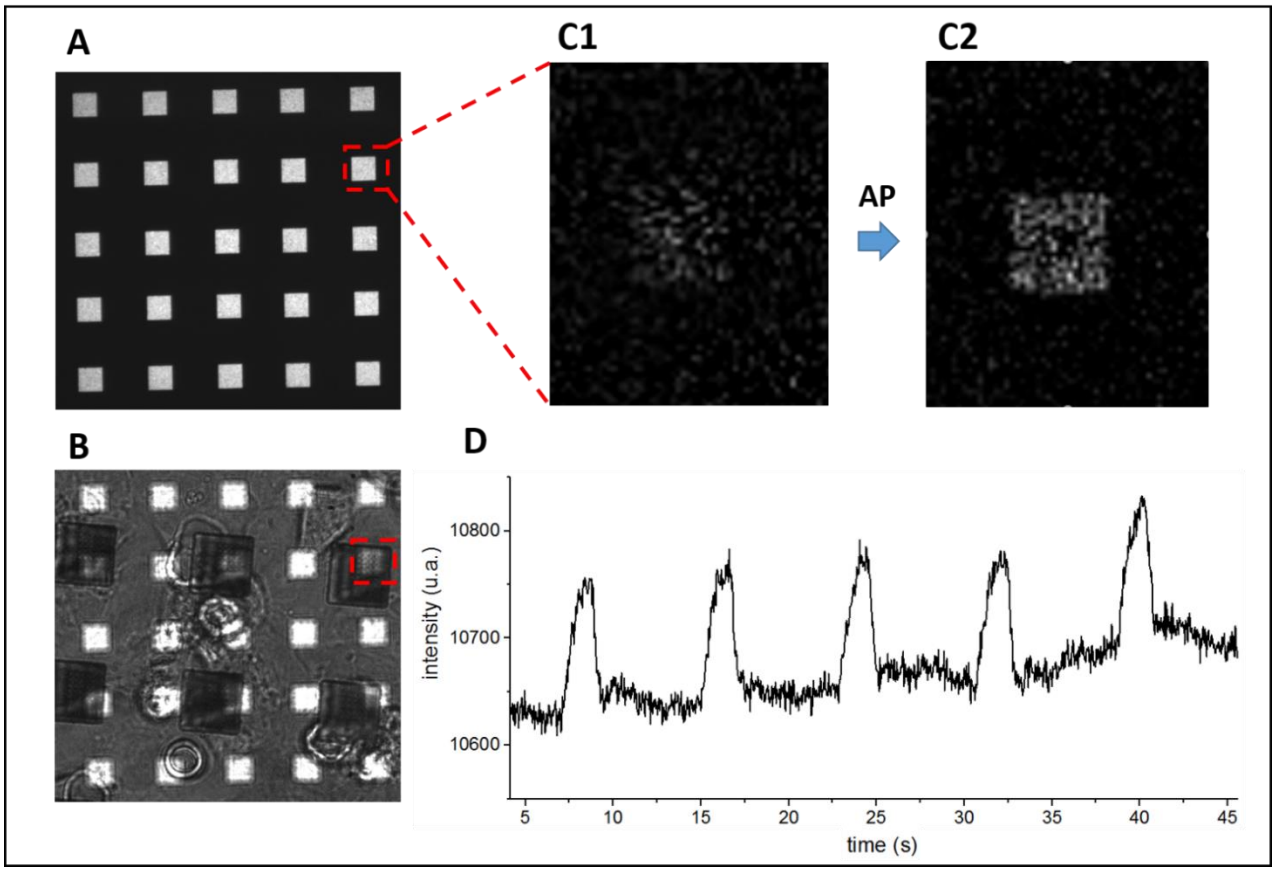

Figure 4.4. Light signature of APs measured with CORE device.
(A) Measured ZMWs arrays. (B) Image of the same region of (A) obtained by turning on the microscope top lamp: it is possible to see that cells were well distributed in the measured region and a good alignment between some top electrode pads and bottom ZMWs arrays was achieved. (C1-C2) Zoomed view, after background subtraction, of a single ZMWs array: a light intensity variation, occurring with the periodicity of cells contractile motion, is visible. (D) Light intensity integrated on the whole highlighted ZMWs array: optical signals clearly emerge, with regular shape and high SNR. (Measurements performed with 60x magnification on Pluricyte cell line – camera acquisition parameters: binning 4x; exposure time = 40 ms).

As discussed in chapter 1, one big advantage given by the optical readout is the possibility to monitor in parallel, i.e. during the same acquisition, more elements, such as all the devices situated in the camera FOV. In Figure 4.5, the APs recorded on different ZMWs arrays are displayed during the same acquisition and time interval: a spatial map of APs light pulses can be drawn.

In the highlighted region, the optical signals detected on the ZMWs arrays that overlap with the top electrode pads have higher amplitude than the ones detected on the ZMWs arrays in between the top electrode pads. This is most likely due to a higher effect of the electric field in the volume beneath the electrode. Nevertheless, amplitude variations between signals can also be due to variabilities in the cell-electrode electrical coupling and the non-physiological external environment that unavoidably affects cells viability and behavior. Moreover, a variability in the device fabrication process, especially in the electrochemical growth of the mushroom-shaped microstructures that form the interface with the cellular culture, can contribute to a different cell-device electrical coupling and thus to the different recorded amplitudes. Finally, some amplitude variations are due to a non-homogeneous illumination of the FOV. Besides this last technical feature, to discriminate between all these factors is not a trivial task.

Apart from the amplitude, optically recorded APs show also some variabilities in their shape and in the sign of the light intensity variation. As for amplitude variability, these two effects can possibly be due to variabilities in the electrical coupling between the cells and the electrodes. They are commonly observed in more conventional recording methods, like MEA and CMOS-MEA recording, as reported in many works in the literature [34].

In contrast to the measurements reported in Figure 4.4, in the sample depicted in Figure 4.5, cells beating rate was around 0.6 Hz: recorded optical signals resulted to follow this new beating rate, giving thus a further confirmation of device functioning. Moreover, the average time duration of AP optical signals at their half amplitude was equal to 500 ms, a value closer to the AP physiological time duration.

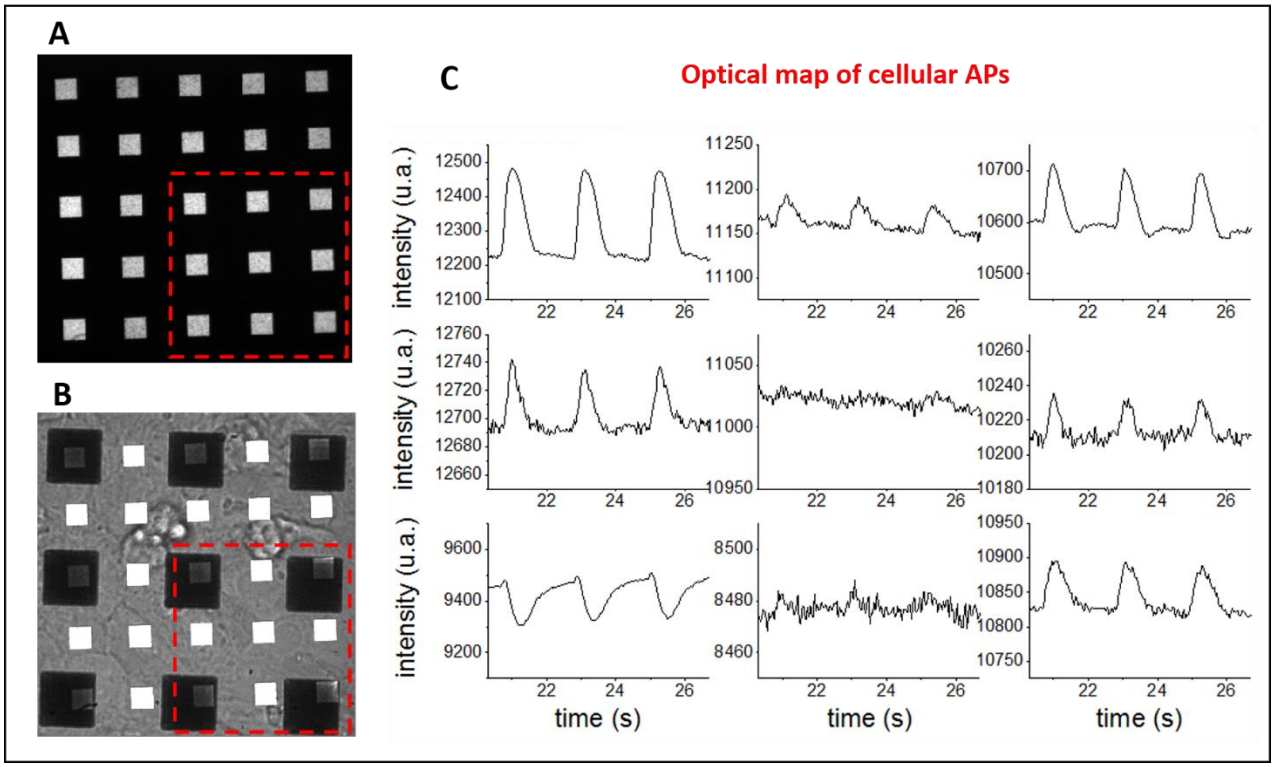

Figure 4.5. Recorded optical map of cellular APs.
(A) Pure fluorescence microscopy image of the measured region. (B) Same region of (A) with microscope top light turned on. (C) APs-associated optical signals recorded on the ZMWs arrays outlined in (A) and (B). An optical map can be drawn: ZMWs arrays underneath the top electrode pads detected higher signals with respect to the ones that do not overlap with the square pads. (Measurements performed with 60x magnification on Cor.4U cell line – camera acquisition parameters: binning 4x; exposure time = 40 ms).

4.1.3.1 Nifedipine drug administration

In order to further explore device behavior and confirm its functioning, a drug, known to alter some features of cellular APs, was administered to the cellular culture during an experiment. The detection of drug effects in the measured AP light pulses can give a further confirmation that the measured optical signals are indeed signature of cellular APs, and thus the device is working properly.

We administered Nifedipine, a molecule known to increase cardiomyocytes beating rate and shorten APs time duration [54]. The drug was administered by adding a small volume of its solution to the cellular medium, with the sample already mounted on the microscope (final Nifedipine concentration in the cellular medium = 90 nM). Few seconds after the administration of the drug, the cells, observed in the modality view of Figure 4.3 A, accelerated their beating activity. In Figure 4.6, the measured optical signals before and after drug administration are compared.

In Figure 4.6 A, it is possible to see that the optical signal rate increases after drug administration: in 16 seconds, the number of detected pulses passed from 10 to 14, meaning that the average pulse frequency increased from 0.63 Hz to 0.88 Hz. In Figure 4.6 B, single light pulses before and after drug administration are compared. The pulse time duration has decreased: the AP duration at half amplitude (APD50) passed from 560 ms to 430 ms, with a reduction of 23%.

These obtained results are in agreement with known Nifedipine effects on cardiomyocytes, as detected by other methods, such as patch-clamp or microelectrode arrays [54], [55]. This experiment is a further confirmation that detected optical signals can be acknowledge as a measure of cellular APs.

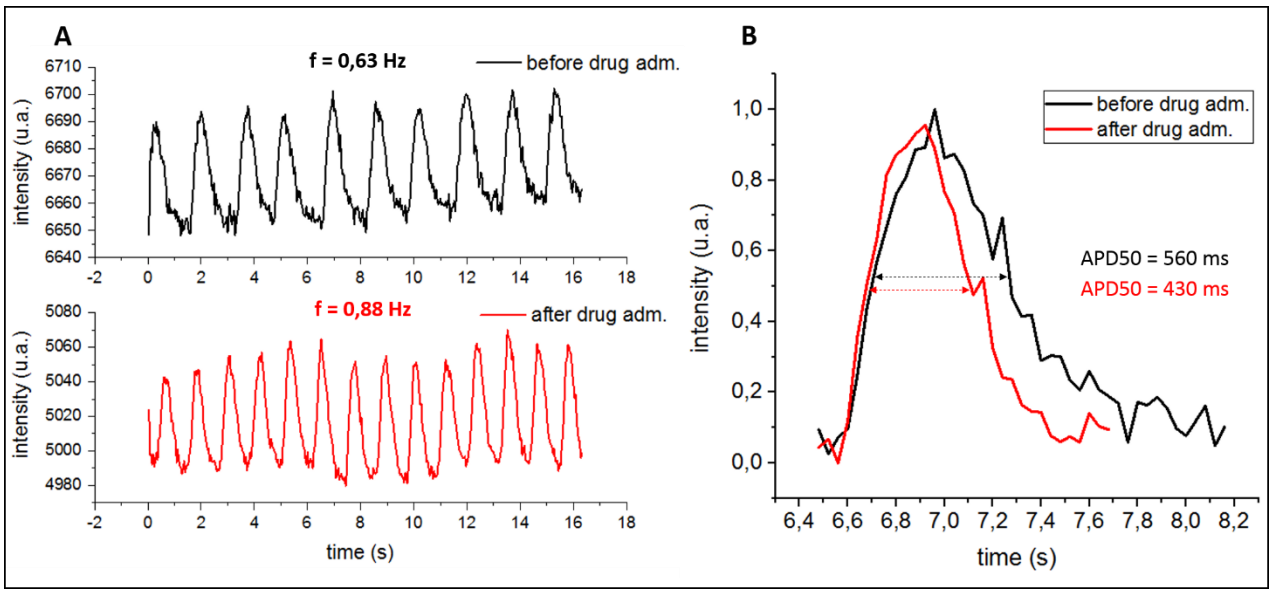

Figure 4.6. Effects of Nifedipine on APs as measured by the CORE device.
Nifedipine was administered to the cellular culture. Light pulses frequency increased after drug administration (A), and their time duration became shorter (B). This experiment is a further evidence that the measured light pulses are indeed signature of cells APs. (Measurements performed with 60x magnification on Cor.4U cell line – camera acquisition parameters: binning 4x; exposure time = 40 ms).

CONCLUSIONS AND PERSPECTIVES

With the continuous progress of technology, an always more accurate collection of scientific data and their efficient processing and storage are becoming crucial in many fields. An important example is given by the biomedical sector, where systems for precise analysis, able to measure a wide range of parameters with sensitivity at the molecular and cellular level, are strongly desired. Future breakthroughs could allow for significant improvements in a broad-spectrum of studies, and the rise of new powerful applications.

In this thesis, a model device was described, which include the potential to answer to such technological challenges. This model device, made by a three layers structure, aims at transducing an electrical stimulus into a variation of the optical response of an active material. As significant advantages, the device structure allows to integrate single elements into high-density, extremely-interconnected arrays. On the other hand, the signal readout performed by an optical camera enables parallel operation.

The device concept was successfully implemented into two different systems. The first device is a new configuration for ZMWs, a photonic nanostructured system that allows to perform optical studies at the single molecule level in highly concentrated fluorophore dispersions. ZMWs are used to monitor, optically, chemical or biochemical reactions: thanks to the optical readout scheme, a parallel detection on a large number of ZMWs can be performed, allowing for very large throughput. This system has been profitably employed for a wide range of applications, among which the sequencing of DNA.

The proposed new device features a pair of electrodes that enclose the fluorophore dispersion to be studied. By applying an electrical voltage between the two electrodes, electrically charged fluorophores can be driven, by the electrophoretic force, inside or outside the ZMWs where the excitation light volume is confined. The corresponding increase or decrease of light intensity emitted from the ZMWs proves the particles motion. As a first result, the possibility to tune fluorophore concentration inside the ZMWs, by applying different amplitude voltages, was successfully demonstrated. This new feature could allow to study, dynamically, a reaction of interest at different molecule concentration levels. As a second result, by applying voltage pulses with different time duration, the possibility to control molecule residence time inside the ZMW was shown. This result proves the possibility to study the reaction of interest, by controlling, moreover, the temporal availability of the fluorescent reagents.

These new features, combined with the known strengths of ZMWs, such as the parallel readout, the high optical efficiency and the easiness of production, can increase significantly the capabilities of the device. This new device, called Electro-Active Zero-Mode Waveguides (EA-ZMWs), is expected to provide a more detailed monitoring of chemical or biochemical processes, giving access to a large spectrum of valuable information, in a simple, cost-effective, and time convenient way.

As a first perspective for the next future, a lock-in technique could be implemented, in order to improve SNR ratio and reduce molecules photobleaching. Moreover, different fluorophore solvents with lower viscosity could be tested, in order to push temporal response down to few ms. Finally, the possibility to test the EA-ZMWs in a real chemical or bio-chemical study is going to be explored. The system could prove favorable for some biochemical trials and new technological applications could arise in the next few years.

The second realization of the device presented in this thesis, is a new system for recording in-vitro the electrical activity of excitable cells, like neurons and cardiomyocytes. The device relies on the detection, by means of arrays of ZMWs, of the vertical motion of fluorescent molecules, induced by the cellular action potentials. The device was first tested by applying external voltage pulses with amplitude and time duration comparable with cellular electrical signals. As a first result, the device was observed to respond to voltage pulses with amplitude and time duration down to 10 mV and 10 ms, and very good quality signals were recorded for voltage pulses compatible with typically recorded intracellular APs. Subsequently, the device was used for experiments with cardiac cells, and distinct optical signals with very high SNR were measured. Through the analysis of their frequency and shape, and by relying on device operation principle, these signals were acknowledged as signature of cardiomyocytes APs. As a further confirmation of device functioning, a drug was administered to the cellular culture, and its effects were measured in the optically recorded APs. As the most representative result, the simultaneous recording on more sites of the cellular culture was achieved, allowing to record optical maps of cellular APs.

The new proposed device, named CORE (Cellular Optical REcording) device, is endowed with a number of advantages with respect to conventional electrical recording methods, such as patch-clamp and MEA/CMOS-MEA recording. In particular, the optical readout performed with a camera allows for the easy parallel recording on the whole cellular culture in the microscope FOV. Moreover, the use of a camera enables to recording with an extremely high spatial resolution, due to the high number of pixel modern camera are endowed with (of the order of millions, three orders of magnitude larger than CMOS-MEA sensors). Finally, while commercial MEA and CMOS-MEA are designed to record

only field potentials (intracellular potentials can be recorded after the post-processing fabrication of 3D nanostructures and the use of electro- or optoacoustic-poration), the electrodes of the CORE system are believed to acquire, being floating electrodes, the actual membrane potential. The AP signal they measure is therefore the actual cellular AP.

In the next future, top electrodes with higher density of square pads are going to be tested. They have pads with size 10 μm and spacing 10 or 30 μm. They will record APs signals on a larger number of sites, allowing, upon reconfiguring the bottom electrode ZMWs arrays, to increase the spatial resolution of the device. As a further improvement, by changing fluorophore solvent, passing to a less viscous one, device response to cellular APs should become faster, and the recorded signal should reproduce more faithfully real APs shape and time duration. The fabrication of a closed microfluidic cell could become necessary in order to avoid solvent evaporation. In this prospect, the implementation of a method for the precise alignment of the top electrode square pads and the bottom electrode ZMWs arrays could improve device operation towards large areas APs recording.

Boosted by these improvements, the realized CORE device aims at being a new, cost-effective system for cellular recording, characterized by parallel operation, high spatial resolution, and actual membrane AP recording. It could be used by pharmaceutical companies, for testing, for example, drug toxicity on cardiac cells, a fundamental step in every drug approval process. Upon further modification, the device could be made soft and flexible, suitable for in-vivo applications. Such applications may refer for example to the brain, where the device could interface with neurons, excitable cells as well. Finally, a large variety of studies, involving AP monitoring, could be performed: they could take advantage of the extraordinarily high spatial resolution this method can provide, allowing for the extremely resolved detection of AP generation and propagation on the cellular membrane.

BIBLIOGRAPHY

[1] D. Reinsel, J. Gantz, and J. Rydning, "Data Age 2025: The Digitization of the World From Edge to Core", *Int. Data Corp.*, no. November, 2018.

[2] S. Lohr, "The Age of Big Data", *New York Times*, 2012.

[3] S. J. Russell and P. Norvig, *Artificial Intelligence: A Modern Approach*, Pearson, 2009.

[4] J. Thompson *et al.*, "5G wireless communication systems: Prospects and challenges", *IEEE Communications Magazine*, vol. 52, no. 2, pp. 62–64, 2014.

[5] J. Luo, M. Wu, D. Gopukumar, and Y. Zhao, "Big Data Application in Biomedical Research and Health Care: A Literature Review", *Biomed. Inform. Insights*, vol. 8, pp. 1-10, 2016.

[6] D. Ielmini and H. S. P. Wong, "In-memory computing with resistive switching devices", *Nat. Electron.*, vol. 1, no. 6, pp. 333–343, 2018.

[7] Y. Van De Burgt, A. Melianas, S. T. Keene, G. Malliaras, and A. Salleo, "Organic electronics for neuromorphic computing", *Nat. Electron.*, vol. 1, no. 7, pp. 386–397, 2018.

[8] M. M. Waldrop, "More Than Moore", *Nature*, vol. 530, pp. 144–147, 2016.

[9] M. Horowitz, "Computing's energy problem (and what we can do about it)", *Dig. Tech. Pap. - IEEE Int. Solid-State Circuits Conf.*, vol. 57, pp. 10–14, 2014.

[10] G. N. Angotzi *et al.*, "SiNAPS: An implantable active pixel sensor CMOS-probe for simultaneous large-scale neural recordings", *Biosens. Bioelectron.*, vol. 126, pp. 355–364, 2019.

[11] F. Santoro *et al.*, "Revealing the Cell-Material Interface with Nanometer Resolution by Focused Ion Beam/Scanning Electron Microscopy", *ACS Nano*, vol. 11, no. 8, pp. 8320–8328, 2017.

[12] D. B. Strukov, G. S. Snider, D. R. Stewart, and R. S. Williams, "The missing memristor found", *Nature*, vol. 453, pp. 80–83, 2008.

[13] S. Pi *et al.*, "Memristor crossbar arrays with 6-nm half-pitch and 2-nm critical dimension", *Nat. Nanotechnol.*, vol. 14, no. 1, pp. 35–39, 2019.

[14] N. Yu and F. Capasso, "Flat optics with designer metasurfaces", *Nat. Mater.*, vol. 13, no. 2, pp. 139–150, 2014.

[15] T. Cui, B. Bai, and H. B. Sun, “Tunable Metasurfaces Based on Active Materials”, *Adv. Funct. Mater.*, vol. 29, no. 10, pp. 1–14, 2019.

[16] Z. Ma, X. Meng, X. Liu, G. Si, and Y. J. Liu, “Liquid crystal enabled dynamic nanodevices”, *Nanomaterials*, vol. 8, no. 11, pp. 1–21, 2018.

[17] M. Wuttig, H. Bhaskaran, and T. Taubner, “Phase-change materials for non-volatile photonic applications”, *Nat. Photonics*, vol. 11, no. 8, pp. 465–476, 2017.

[18] C. G. Granqvist, M. A. Arvizu, Bayrak Pehlivan, H. Y. Qu, R. T. Wen, and G. A. Niklasson, “Electrochromic materials and devices for energy efficiency and human comfort in buildings: A critical review”, *Electrochim. Acta*, vol. 259, pp. 1170–1182, 2018.

[19] Y. Montelongo *et al.*, “Electrotunable nanoplasmonic liquid mirror”, *Nat. Mater.*, vol. 16, no. 11, pp. 1127–1135, 2017.

[20] A. Barik, X. Chen, and S. H. Oh, “Ultralow-Power Electronic Trapping of Nanoparticles with Sub-10 nm Gold Nanogap Electrodes”, *Nano Lett.*, vol. 16, no. 10, pp. 6317–6324, 2016.

[21] K. Thyagarajan, R. Sokhoyan, L. Zornberg, and H. A. Atwater, “Millivolt Modulation of Plasmonic Metasurface Optical Response via Ionic Conductance”, *Adv. Mater.*, vol. 29, no. 31, pp. 1–8, 2017.

[22] H. J. Levene, J. Korlach, S. W. Turner, M. Foquet, H. G. Craighead, and W. W. Webb, “Zero-mode waveguides for single-molecule analysis at high concentrations”, *Science*, vol. 299, no. 5607, pp. 682–686, 2003.

[23] G. M. Crouch, D. Han, and P. W. Bohn, “Zero-mode waveguide nanophotonic structures for single molecule characterization”, *J. Phys. D. Appl. Phys.*, vol. 51, no. 19, 2018.

[24] P. Ponzellini, X. Zambrana-Puyalto, N. Maccaferri, L. Lanzanò, F. De Angelis, and D. Garoli, “Plasmonic zero mode waveguide for highly confined and enhanced fluorescence emission”, *Nanoscale*, vol. 10, no. 36, pp. 17362–17369, 2018.

[25] J. K. Trauman, J. J. Macklin, L. E. Brus, and E. Betzig, “Near-field spectroscopy of single molecules at room temperature”, *Nature*, vol. 369, pp. 40–42, 1994.

[26] M. Tokunaga, K. Kitamura, K. Saito, A. H. Iwane, and T. Yanagida, “Single Molecule Imaging of Fluorophores and Enzymatic Reactions Achieved by Objective-Type Total Internal Reflection Fluorescence Microscopy”, *Biochem. Biophys. Res. Commun.*, vol. 53, no. 235, pp.

47–53, 1997.

[27] D. M. Bers, “Cardiac excitation–contraction coupling”, *Nature*, vol. 415, no. January, pp. 198–205, 2002.

[28] J. Pinnell, S. Turner, and S. Howell, “Cardiac muscle physiology”, *Contin. Educ. Anaesthesia, Crit. Care Pain*, vol. 7, no. 3, pp. 85–88, 2007.

[29] J. M. Nerbonne and R. S. Kass, “Molecular physiology of cardiac repolarization”, *Physiol. Rev.*, vol. 85, no. 4, pp. 1205–1253, 2005.

[30] B. D. Anson, K. L. Kolaja, and T. J. Kamp, “Opportunities for Human iPS Cells in Predictive Toxicology”, *Clin Pharmacol Ther.*, vol. 89, no. 5, pp. 754–758, 2011.

[31] L. G. J. Tertoolen, S. R. Braam, B. J. van Meer, R. Passier, and C. L. Mummery, “Interpretation of field potentials measured on a multi electrode array in pharmacological toxicity screening on primary and human pluripotent stem cell-derived cardiomyocytes”, *Biochem. Biophys. Res. Commun.*, vol. 497, no. 4, pp. 1135–1141, 2018.

[32] O. P. Hamill, A. Marty, E. Neher, B. Sakmann, and F. J. Sigworth, “Improved patch-clamp techniques for high-resolution current recording from cells and cell-free membrane patches”, *Pflügers Arch. Eur. J. Physiol.*, vol. 391, no. 2, pp. 85–100, 1981.

[33] P. Connolly, P. Clark, A. S. G. Curtis, J. A. T. Dow, and C. D. W. Wilkinson, “An Extracellular microelectrode array for monitoring electrogenic cells in culture”, *Biosens. Bioelectron.*, vol. 5, no. 3, pp. 223–234, 1990.

[34] J. Müller *et al.*, “High-resolution CMOS MEA platform to study neurons at subcellular, cellular, and network levels”, *Lab Chip*, vol. 15, no. 13, pp. 2767–2780, 2015.

[35] R. Capozza *et al.*, “Cell Membrane Disruption by Vertical Micro-/Nanopillars: Role of Membrane Bending and Traction Forces”, *ACS Appl. Mater. Interfaces*, vol. 10, pp. 29107–29114, 2018.

[36] B. X. E. Desbiolles, E. De Coulon, A. Bertsch, S. Rohr, and P. Renaud, “Intracellular Recording of Cardiomyocyte Action Potentials with Nanopatterned Volcano-Shaped Microelectrode Arrays”, *Nano Lett.*, vol. 19, no. 9, pp. 6173–6181, 2019.

[37] C. Xie, Z. Lin, L. Hanson, Y. Cui, and B. Cui, “Intracellular recording of action potentials by nanopillar electroporation”, *Nat. Nanotechnol.*, vol. 7, no. 3, pp. 185–190, 2012.

[38] J. Abbott *et al.*, “CMOS nanoelectrode array for all-electrical intracellular electrophysiological imaging”, *Nat. Nanotechnol.*, vol. 12, no. 5, pp. 460–466, 2017.

[39] M. Dipalo *et al.*, “Intracellular and Extracellular Recording of Spontaneous Action Potentials in Mammalian Neurons and Cardiac Cells with 3D Plasmonic Nanoelectrodes”, *Nano Lett.*, vol. 17, no. 6, pp. 3932–3939, 2017.

[40] M. Dipalo *et al.*, “Plasmonic meta-electrodes allow intracellular recordings at network level on high-density CMOS-multi-electrode arrays”, *Nat. Nanotechnol.*, vol. 13, no. 10, pp. 965–971, 2018.

[41] F. Santoro *et al.*, “Interfacing electrogenic cells with 3D nanoelectrodes: Position, shape, and size matter”, *ACS Nano*, vol. 8, no. 7, pp. 6713–6723, 2014.

[42] P. Atkins, J. De Paula, and J. Keeler, *Physical Chemistry*, Oxford University Press, 2017.

[43] T. Jacob and L. Sabo, *Electrochemical Double Layer*, Elsevier Inc., 2018.

[44] A. J. Bard and L. R. Faulkner, *Electrochemical Methods*, John Wiley & Sons, 2001.

[45] M. E. Spira and A. Hai, “Multi-electrode array technologies for neuroscience and cardiology”, *Nat. Nanotechnol.*, vol. 8, no. 2, pp. 83–94, 2013.

[46] A. Cerea *et al.*, “Coaxial-like three-dimensional nanoelectrodes for biological applications”, *Microelectron. Eng.*, vol. 187–188, pp. 21–26, 2018.

[47] S. Weidlich, K. J. Krause, J. Schnitker, B. Wolfrum, and A. Offenhäusser, “MEAs and 3D nanoelectrodes: Electrodeposition as tool for a precisely controlled nanofabrication”, *Nanotechnology*, vol. 28, no. 9, pp. 1–8, 2017.

[48] F. M. Zehentbauer *et al.*, “Fluorescence spectroscopy of Rhodamine 6G: Concentration and solvent effects”, *Spectrochim. Acta - Part A Mol. Biomol. Spectrosc.*, vol. 121, pp. 147–151, 2014.

[49] J. Ma *et al.*, “High purity human-induced pluripotent stem cell-derived cardiomyocytes: Electrophysiological properties of action potentials and ionic currents”, *Am. J. Physiol. - Hear. Circ. Physiol.*, vol. 301, no. 5, pp. 2006–2017, 2011.

[50] K. Drews, J. Jozefczuk, A. Prigione, and J. Adjaye, “Human induced pluripotent stem cells-from mechanisms to clinical applications”, *J. Mol. Med.*, vol. 90, no. 7, pp. 735–745, 2012.

[51] C. Denning *et al.*, “Cardiomyocytes from human pluripotent stem cells: From laboratory curiosity to industrial biomedical platform”, *Biochim. Biophys. Acta - Mol. Cell Res.*, vol. 1863, no. 7, pp. 1728–1748, Jul. 2016.

[52] P. O. Gendron, F. Avaltroni, and K. J. Wilkinson, “Diffusion coefficients of several rhodamine derivatives as determined by pulsed field gradient-nuclear magnetic resonance and fluorescence correlation spectroscopy”, *J. Fluoresc.*, vol. 18, no. 6, pp. 1093–1101, 2008.

[53] M. Dipalo *et al.*, “Cells Adhering to 3D Vertical Nanostructures: Cell Membrane Reshaping without Stable Internalization”, *Nano Lett.*, vol. 18, no. 9, pp. 6100–6105, 2018.

[54] K. Harris, M. Aylott, Y. Cui, J. B. Louttit, N. C. Mcmahon, and A. Sridhar, “Comparison of Electrophysiological Data From Human-Induced Pluripotent Stem Cell-Derived Cardiomyocytes to Functional Preclinical Safety Assays”, *Toxicol. Sci.*, vol. 134, no. 2, pp. 412–426, 2013.

[55] S. Peng, A. E. Lacerda, G. E. Kirsch, A. M. Brown, and A. Bruening-Wright, “The action potential and comparative pharmacology of stem cell-derived human cardiomyocytes”, *J. Pharmacol. Toxicol. Methods*, vol. 61, no. 3, pp. 277–286, 2010.

ACKNOWLEDGEMENTS

At the end of my PhD experience, I want to express here my gratitude to my supervisor dr. Francesco De Angelis, who gave me the big opportunity to work in his group and join a very dynamic and international context, such as the Italian Institute of Technology. It has been an extraordinary experience, shared with great people, working on fascinating research topics. I thank you for the patience that you show me while I was "gaining experience" in the laboratory work. I thank you also for all the meetings that we had, where I felt your support and, very importantly, your true passion for science that you were able to convey to me.

I want to say a very big thanks to Michele Dipalo. You taught me the basics of a large part of the laboratory work and you were always present to discuss about new experiments and results. You gave me very good advice during all these years, and it has been always a pleasure to work with you. These few lines are not sufficient to express my gratitude for you.

A great thanks goes to Francesco Tantussi and Andrea Toma, for their valuable support, both scientific and personal. Thank you for all the advice and suggestions that you gave me, and for all the time that you spent discussing with me about my project. For sure, you helped me in growing both professionally and personally.

I would like to thank all the people, PhD students and Post-Docs, that have been part of the Plasmon Nanotechnologies group during all these years. You are many, I cannot mention all of you. I just want to say that it was really a pleasure to meet each of you. Thank you especially for all the very good moments spent together, both in the labs and outside in the city.

A special thanks to the Cleanroom technicians, Marco, Eliana, Fabio, Claudio and Alessandro, for your constant and always precious support.

Thanks also to my office mates, in particular Milan, Giulia and Helena, for your kind empathy during all the "ups and downs" of my PhD experience.

I also would like to thank my lifelong friends Beniamino, Alessia, Fabrizio and Albina, for your constant, close and intense friendship that I felt during all these years. Thanks also to all the beautiful new friends met in Genova, especially Simona, Luca, Lucia and Donatella. It was great to share many beautiful experiences with you at this stage of my life.

An enormous thanks to my housemates, Eder and Davide, for your patience and friendship. A musician and a pastry chef. What could I ask for more?

Finally, the most important thanks is for my family, simply for your stubborn, incredible love.